

A staggered discontinuous Galerkin method for the simulation of seismic waves with surface topography

Eric T. Chung¹, Chi Yeung Lam¹, and Jianliang Qian²

ABSTRACT

Accurate simulation of seismic waves is of critical importance in a variety of geophysical applications. Based on recent works on staggered discontinuous Galerkin methods, we have developed a new method for the simulations of seismic waves, which has energy conservation and extremely low grid dispersion, so that it naturally provided accurate numerical simulations of wave propagation useful for geophysical applications and was a generalization of classical staggered-grid finite-difference methods. Moreover, it could handle with ease irregular surface topography and discontinuities in the subsurface models. Our new method discretized the velocity and the stress tensor on this staggered grid, with continuity imposed on different parts of the mesh. The symmetry of the stress tensor was enforced by the Lagrange multiplier technique. The resulting method was an

explicit scheme, requiring the solutions of a block diagonal system and a local saddle point system in each time step, and it was, therefore, very efficient. To tailor our scheme to Rayleigh waves, we developed a mortar formulation of our method. Specifically, a fine mesh was used near the free surface and a coarse mesh was used in the rest of the domain. The two meshes were in general not matching, and the continuity of the velocity at the interface was enforced by a Lagrange multiplier. The resulting method was also efficient in time marching. We also developed a stability analysis of the scheme and an explicit bound for the time step size. In addition, we evaluated some numerical results and found that our method was able to preserve the wave energy and accurately computed the Rayleigh waves. Moreover, the mortar formulation gave a significant speed up compared with the use of a uniform fine mesh, and provided an efficient tool for the simulation of Rayleigh waves.

INTRODUCTION

Accurate simulation of seismic and Rayleigh waves is of critical importance in a variety of geophysical applications, such as exploration geophysics, geotechnical characterization, and earthquake-related damage assessment (Aki and Richards, 2002). Consequently, it is a long-studied topic in geophysics in that many challenging problems arise in designing for Rayleigh wave simulation, an accurate method which ideally should enjoy low grid dispersion, provide accurate long-time/long-range wave propagation, and allow irregular surface topography and discontinuities in the subsurface model. Based on recent works by Chung and Engquist (2006, 2009), we designed a staggered discontinuous Galerkin (DG) method to tackle exactly these challenges: The new method has extremely low grid dispersion as shown by Chung et al. (2013a) and Chan et al. (2013);

it has the energy-conservation property (Chung and Engquist, 2006, 2009), so that it naturally provides accurate numerical simulations of wave propagation useful for geophysical applications and is a generalization of classical staggered-grid finite-difference methods (FDMs). Moreover, it can handle with ease irregular surface topography and discontinuities in the subsurface models because our method is based on a novel triangular staggered mesh.

In the literature, simulations of Rayleigh waves have been mainly tackled with FDMs and finite-element methods (FEMs). In terms of FDMs for Rayleigh waves, most of these methods are based on staggered-grid FDMs proposed by Madariaga (1976), Virieux (1986), and Levander (1988). When the surface topography is flat, the free-surface boundary condition associated with Rayleigh waves is relatively easy to handle in a staggered-grid FDM. In Bohlen and Saenger (2006), the staggered-grid and the rotated

Manuscript received by the Editor 29 August 2014; revised manuscript received 26 February 2015; published online 29 May 2015.

¹The Chinese University of Hong Kong, Department of Mathematics, Hong Kong SAR, The People's Republic of China. E-mail: tschung@math.cuhk.edu.hk; cylam@math.cuhk.edu.hk.

²Michigan State University, Department of Mathematics, East Lansing, Michigan, USA. E-mail: qian@math.msu.edu.

© 2015 Society of Exploration Geophysicists. All rights reserved.

staggered-grid FDMs are applied to simulate Rayleigh waves with flat surface topography, and accuracy for both methods is carefully studied. It is well known that one needs more points per wavelength for surface waves than body waves because the surface wave in the case of flat topography mainly travels horizontally and decays exponentially in the vertical direction. Therefore, one needs to use more points in the vertical direction to capture the sharp decay. To overcome this increase in the number of unknowns near the surface, [Kosloff and Carcione \(2010\)](#) propose a variable-grid-spacing method, in which the spatial grid is finer near the surface and coarser far away from the surface, and the staggered sine and cosine transforms are applied to compute spatial derivatives; the resulting method is highly accurate and is able to handle propagation of Rayleigh waves at large offsets.

When the surface topography is nonflat, two remedies are proposed to treat free-surface boundary conditions in the setting of a staggered-grid FDM: One option is to use a staircase approximation to the nonflat free-surface topography; another option is to match the free-surface topography by deforming computational grids. When applying the staircase approximation to the nonflat free surface topography, [Levander \(1988\)](#) originally proposes the stress-image technique to update the velocities for grid nodes on (flat) free surfaces, and [Robertsson \(1996\)](#) proposes an extension of this method, in which the grid nodes are classified into seven categories with different update rules. The vacuum formulation ([Zahradnik et al., 1993](#)) is developed along the same line by setting parameters to zero above the free surface, so that surface topography can be implemented in the same manner as an internal material interface. However, numerical tests have shown that the simple vacuum formulation becomes unstable when using fourth-order or higher order spatial difference operators ([Graves, 1996](#)). Consequently, [Zeng et al. \(2012\)](#) propose an improved vacuum formulation to incorporate surface topography, in which the parameters at the surface grid nodes are averaged using the same scheme as for the interior grid nodes; this method is shown to be stable using fourth-order spatial difference operators without notable numerical dispersion. On the other hand, various methods are proposed to deform computational grids to match the free surface topography by curvilinear coordinates: [Hestholm and Ruud \(2002\)](#), [Zhang and Chen \(2006\)](#), and [Lombard et al. \(2008\)](#) in the setting of a staggered-grid FDM and [Appelö and Petersson \(2009\)](#) in the setting of a nonstaggered-grid FDM. Because these methods involve computation of spatial derivatives in the curved grid and application of the chain rule to calculate the required Cartesian spatial derivatives, [Komatitsch et al. \(1996\)](#) propose a method to solve the equation directly on curved grids.

Despite the efficiency of FDMs on structured grids, implementing free-surface conditions in FDMs can be difficult on an irregular domain. Therefore, [Moczo et al. \(1997\)](#) present a hybrid method, in which low-order FEMs were used near boundaries, whereas second-order FDMs were used for the rest of the model, and [Ma et al. \(2004\)](#) present another hybrid method, which combines low-order FEMs with a fourth-order velocity-stress staggered-grid FDM. There are certainly plenty of advantages in using FEMs for surface topography because they allow the use of triangular meshes suitable for irregular surfaces. In terms of new developments in FEM for seismic wave modeling, several different methods are popular in the geophysical community as briefly summarized in [Basabe and Sen \(2009\)](#): the mixed FEM, the spectral-element method (SEM), and

the DG method. [Raviart and Thomas \(1977\)](#) introduce the mixed FEM, which is suitable for the spatial approximation of the wave equation in the velocity-stress form, and [Geveci \(1988\)](#) analyzes its convergence. The advantage of using mixed formulations is that the energy is conserved locally and globally, which is an important property described by wave equations. However, when an explicit time discretization is applied, this method usually produces an implicit time-marching scheme because nondiagonal mass matrices may arise in the process, which makes the explicit time-stepping inefficient. The mass-lumping technique, which is a way to approximate the mass matrix by a diagonal matrix, is developed to improve the efficiency ([Becache et al., 2000](#); [Cohen et al., 2001](#)). However, a mass-lumping technique for tetrahedral meshes is not available for an arbitrary order of approximations. The SEM is a class of high-order Galerkin FEMs and was originally developed for fluid dynamics ([Patera, 1984](#)), and it has been successfully applied to acoustic- and elastic-wave propagations ([Seriani and Priolo, 1994](#); [Komatitsch and Vilotte, 1998](#); [Komatitsch et al., 2008](#)). Being a method designed for hexahedral meshes, the SEM makes the design of an optimal mesh cumbersome in contrast to the flexibility offered by tetrahedral meshes. The DG FEMs provide another class of methods that can overcome the above disadvantages. In particular, DG FEMs are constructed based on tetrahedral meshes, and they have block diagonal mass matrices due to the discontinuous nature of basis functions, allowing efficient time marching. The DG method was first introduced for the neutron transport equation by [Reed and Hill \(1973\)](#) and [Lesaint and Raviart \(1974\)](#). Since then, the method has become very popular for the numerical solutions of partial differential equations. For a general introduction to the subject, see [Arnold \(1982\)](#), [Riviere \(2008\)](#), and [Cockburn et al. \(2000\)](#). Regarding computational wave propagation, some DG methods are proposed by [Bernacki et al. \(2006\)](#), [Bourdel et al. \(1991\)](#), [Giraldo et al. \(2002\)](#), [Grote et al. \(2006\)](#), and [Hu et al. \(1999\)](#) for the acoustic-wave equations and by [Falk and Richter \(1999\)](#) and [Johnson and Pitkänta \(1986\)](#) for the hyperbolic system. For seismic wave simulations, some DG methods are proposed by [Rivière and Wheeler \(2003\)](#), [Dumbser and Kaser \(2006\)](#), and [De Basabe et al. \(2008\)](#). Furthermore, the dispersive and dissipative properties of the DG methods are analyzed by [Ainsworth et al. \(2006\)](#) and [Chan et al. \(2013\)](#). Recently, a new class of staggered DG (SDG) methods based on staggered meshes was proposed and analyzed. In particular, the SDG method has been successfully developed for many wave propagation problems ([Chung and Engquist, 2006, 2009](#); [Chung and Lee, 2012](#); [Chan et al., 2013](#); [Chung and Ciarlet, 2013](#); [Chung et al., 2013a](#)) and other applications ([Chung et al., 2013b, 2014a, 2014b](#); [Kim et al., 2013, 2014](#); [Chung and Kim, 2014](#)). The SDG method is typically applied to the first-order formulation of wave equations, and it starts with two sets of irregular, staggered grids for each of the two unknown functions involved; furthermore, it designs two finite-element spaces on those two sets of staggered grids and carries out integration-by-parts to derive corresponding weak formulations; and finally, it applies the standard leap-frog scheme for explicit time stepping. The SDG method has several distinctive features that are particularly attractive: First, it conserves the wave energy automatically; second, it is optimally convergent in the L^2 -norm and energy norm; third, it yields block-diagonal mass matrices, so that very efficient explicit time stepping is allowed; fourth, it is flexible in handling complex geometries, so that free surface conditions on nonflat surfaces can be imposed

easily; and fifth, as shown in Chung et al. (2013a) and Chan et al. (2013), it yields solutions with extremely low dispersion errors in that the order of dispersion error in terms of grid size for the SDG method is two orders higher than that of classical FDMs based on nonstaggered grids. Because the SDG method offers many advantages in computational wave propagation, it provides a competitive alternative for simulations of Rayleigh waves and seismic waves in general for models with irregular surface topography. It is, therefore, the purpose of this paper to develop an SDG method for the elastic-wave equation. We emphasize that the SDG method for the acoustic-wave equation, for example, Chung and Engquist (2006, 2009), cannot be directly applied to the elastic-wave equation due to the symmetry of the stress tensor. In this paper, we construct a new SDG method using the Lagrange multiplier technique for the enforcement of the symmetry of the stress tensor. The resulting scheme retains all the advantages of the SDG method for acoustic-wave equations discussed above. Moreover, due to the staggered continuity property of basis functions for the SDG method, the use of the Lagrange multiplier only gives a local saddle point system, instead of a global system common to other Lagrange multiplier techniques for FEMs. Hence, the time marching can be done very efficiently. In addition, a mortar formulation is developed to tailor our scheme to the simulation of Rayleigh waves. We split the computational domain in two parts, one of which is a thin layer near the free surface. A very fine mesh is used in the thin layer near the surface to capture the Rayleigh wave, and a coarse mesh is used in the rest of the domain to speed up the simulations. The basis functions for the velocity in the two parts of the computational domain are totally decoupled, and they are connected by the use of the Lagrange multiplier. The resulting scheme is able to produce an equally accurate solution compared with the solution obtained by a uniform fine mesh. The paper is organized as follows: We start with the basic formulation of the SDG method, followed by a stability analysis for the time step size. A set of numerical results is then given to show the performance of the scheme. In addition, a numerical study of the dispersion error is presented. Finally, a mortar formulation is developed to tailor the scheme to Rayleigh waves. We end with a conclusion.

PROBLEM SETTING

The simulation of Rayleigh waves is mathematically modeled by a half-space problem. To simplify the presentation, we will consider the 2D problems only. First, the domain of interest is the infinite half-space defined by

$$\hat{\Omega} := \{(x, z) \mid -\infty < x < \infty, \Gamma(x) < z < \infty\}, \quad (1)$$

where $\Gamma(x)$ is a function that models the surface topography. In the domain $\hat{\Omega}$, we solve the following elastic-wave equation:

$$\rho \frac{\partial \mathbf{u}}{\partial t} - \operatorname{div} \boldsymbol{\Sigma} = \mathbf{f}, \quad (2)$$

$$\mathbf{A} \frac{\partial \boldsymbol{\Sigma}}{\partial t} - \boldsymbol{\varepsilon}(\mathbf{u}) = 0, \quad (3)$$

where ρ is the density, $\mathbf{u} = (u_1, u_2)^T$ is the velocity field, and $\boldsymbol{\Sigma} = (\sigma_{ij})$ is the 2×2 symmetric stress tensor. In addition, $\mathbf{f} = (f_1, f_2)^T$

is a given source term. We write $\boldsymbol{\sigma}_1 = (\sigma_{11}, \sigma_{12})$ and $\boldsymbol{\sigma}_2 = (\sigma_{21}, \sigma_{22})$ as the first and the second rows of $\boldsymbol{\Sigma}$, respectively. The above divergence is defined as $\operatorname{div} \boldsymbol{\Sigma} = (\operatorname{div} \boldsymbol{\sigma}_1, \operatorname{div} \boldsymbol{\sigma}_2)^T$. Moreover, we have $\boldsymbol{\varepsilon}(\mathbf{u})_{ij} = \frac{1}{2}(\partial_i u_j + \partial_j u_i)$. Matrix \mathbf{A} is defined by

$$\mathbf{A} = \begin{pmatrix} \lambda + 2\mu & \lambda & 0 & 0 \\ \lambda & \lambda + 2\mu & 0 & 0 \\ 0 & 0 & 2\mu & 0 \\ 0 & 0 & 0 & 2\mu \end{pmatrix}^{-1}, \quad (4)$$

where we assume that $\boldsymbol{\Sigma} = (\sigma_{11}, \sigma_{22}, \sigma_{12}, \sigma_{21})^T$ in equation 3; λ and μ are the first and second Lamé parameters of the material. Introducing a skew-symmetric 2×2 matrix $\boldsymbol{\Gamma}$, we have

$$\rho \frac{\partial \mathbf{u}}{\partial t} - \operatorname{div} \boldsymbol{\Sigma} = \mathbf{f}, \quad (5)$$

$$\mathbf{A} \frac{\partial \boldsymbol{\sigma}}{\partial t} - \nabla \mathbf{u} + \boldsymbol{\Gamma} = 0, \quad (6)$$

where

$$\boldsymbol{\Gamma} = (\gamma_{ij}) = \frac{1}{2}(\partial_j u_i - \partial_i u_j). \quad (7)$$

Note that in the 2D setting, the skew-symmetric matrix $\boldsymbol{\Gamma}$ is equivalent to a scalar function γ because the diagonal terms are zero and the off-diagonal terms have the same magnitude with opposite signs. We remark that the role of $\boldsymbol{\Gamma}$ in the SDG method is a Lagrange multiplier to enforce the symmetry of the approximate stress tensor. The details will be explained in the next section. To solve the above elastic-wave equations 5 and 6, we impose suitable initial conditions and the following free-surface boundary condition

$$\boldsymbol{\Sigma} \mathbf{n} = 0 \quad \text{on } z = \Gamma(x), \quad (8)$$

where \mathbf{n} is the outward normal to the free surface and $\boldsymbol{\Sigma} \mathbf{n}$ is the standard matrix-vector product.

We introduce some notations that will be used throughout the paper. For two tensors $\boldsymbol{\Sigma}$ and $\boldsymbol{\alpha}$, we define

$$\boldsymbol{\Sigma} \cdot \boldsymbol{\alpha} = \sum_{i=1}^2 \sum_{j=1}^2 \sigma_{ij} \alpha_{ij}. \quad (9)$$

For a tensor $\boldsymbol{\Sigma}$ and a vector \mathbf{u} , we define

$$\boldsymbol{\Sigma} \cdot \nabla \mathbf{u} = \sum_{i=1}^2 \boldsymbol{\sigma}_i \cdot \nabla u_i, \quad (10)$$

and

$$\mathbf{u} \cdot (\operatorname{div} \boldsymbol{\Sigma}) = \sum_{i=1}^2 u_i (\operatorname{div} \boldsymbol{\sigma}_i). \quad (11)$$

For a unit vector \mathbf{n} , we define

$$\mathbf{u} \cdot (\boldsymbol{\Sigma} \mathbf{n}) = \sum_{i=1}^2 u_i (\boldsymbol{\sigma}_i \cdot \mathbf{n}). \quad (12)$$

THE STAGGERED DISCONTINUOUS GALERKIN METHOD

A staggered triangular grid

We will now present the triangulation of the domain by an unstructured staggered grid. Let Ω be the computational domain, which is a truncation of the infinite half-space $\bar{\Omega}$ and is defined by

$$\Omega = \{(x, z) \mid -R < x < R, \Gamma(x) < z < L\}. \quad (13)$$

We assume that Ω is triangulated by an initial triangular mesh, called \mathcal{T}_h' . This mesh can be formed by any mesh generator. For each triangle in this mesh, we choose an interior point ν , and then we subdivide each triangle into three subtriangles by connecting this point ν to the three vertices of the triangle. A new mesh, called \mathcal{T}_h , is then formed by this subdivision process. That is, \mathcal{T}_h is the refined triangulation of \mathcal{T}_h' defined by the above construction. The set of all these nodes ν is denoted by \mathcal{N} . An example of such construction is illustrated in Figure 1. The triangles of the initial triangulation \mathcal{T}_h' are denoted by solid lines. The newly formed edges are denoted by dotted lines.

Next, we define two types of macroelement. The first type of macroelements is defined with respect to the initial mesh. In particular, the triangles of the initial mesh \mathcal{T}_h' are called the *first-type macroelements*. We use $\mathcal{S}(\nu)$ to denote such a macroelement, and we remark that these elements are parametrized by ν . An example of such an element is illustrated by the shaded region with horizontal lines in Figure 1. The second type of macroelement is defined with respect to the edges of the initial triangulation \mathcal{T}_h' , and we use $\mathcal{R}(\kappa)$ to denote such a macroelement. The macroelement $\mathcal{R}(\kappa)$ is defined as the union of the two triangles in \mathcal{T}_h sharing the edge κ . An example of such an element is illustrated by the shaded region with vertical lines in Figure 1. If an edge κ of the initial triangulation lies on the boundary of the computational domain, then we define $\mathcal{R}(\kappa)$

to be the only triangle in \mathcal{T}_h having the edge κ . Moreover, we use the notation \mathcal{F}_u to represent the set of edges of the initial triangulation and \mathcal{F}_u^0 the subset of interior edges because u will be defined to be continuous across those edges. We use the notation \mathcal{F}_σ to denote the set of new edges formed by the above subdivision process because the normal components of σ will be defined to be continuous across those new edges.

Let $m \geq 1$ be a nonnegative integer representing the order of polynomials used in our approximation space. For any triangle τ in the triangulation \mathcal{T}_h , we let $P^m(\tau)$ be the space of polynomials of degree at most m defined on τ . We define P^m as the space of piecewise $P^m(\tau)$ functions; that is, $v \in P^m$ if the restriction of v on each triangle $\tau \in \mathcal{T}_h$ is in $P^m(\tau)$. We remark that we do not impose any continuity of functions in P_m on the edges of the triangulation \mathcal{T}_h .

Next, we present definitions of the approximation spaces. First, we introduce the function space $(U_h)^2$ for the approximation of the velocity vector \mathbf{u} . Each component of \mathbf{u} belongs to the space U_h , which is defined by

$$U_h = \{v \in P^m \mid v \text{ is continuous on } \mathcal{F}_u^0\}. \quad (14)$$

Thus, the functions in the space U_h are polynomials of at most degree m on each triangle $\tau \in \mathcal{T}_h$, such that they are continuous across the internal edges of the initial triangulation \mathcal{T}_h' , namely, the set \mathcal{F}_u^0 . Because the functions in U_h are in general discontinuous on \mathcal{F}_σ , these functions are supported on $\mathcal{R}(\kappa)$, the second-type of macroelement. Second, we introduce the function space $(W_h)^2$ for the approximation of $\boldsymbol{\Sigma}$. The vectors $\boldsymbol{\sigma}_1$ and $\boldsymbol{\sigma}_2$ belong to the space W_h , which is defined by

$$W_h = \{\boldsymbol{\alpha} \in (P^m)^2 \mid \boldsymbol{\alpha} \cdot \mathbf{n} \text{ is continuous on } \mathcal{F}_\sigma\}. \quad (15)$$

The vector fields in the space W_h are polynomials of degree at most m on each triangle $\tau \in \mathcal{T}_h$, such that the normal components on the set of edges \mathcal{F}_σ are continuous. Because the vector fields in W_h are in general discontinuous on \mathcal{F}_u^0 , these vectors are supported on $\mathcal{S}(\nu)$, the first-type of macroelement. Finally, we introduce the function space X_h for the approximation of the function Γ . We will take $X_h = P^{m-1}$, which contains functions that are discontinuous on all edges in the triangulation \mathcal{T}_h .

Derivation

We will now derive the SDG method for the approximation of equations 5 and 6. We consider the first component of equation 5; namely

$$\rho \frac{\partial u_1}{\partial t} - \text{div } \boldsymbol{\sigma}_1 = f_1. \quad (16)$$

Let v_1 be a smooth test function. Multiplying equation 16 by the test function v_1 and integrating on $\mathcal{R}(\kappa)$ yields

$$\begin{aligned} & \int_{\mathcal{R}(\kappa)} \rho \frac{\partial u_1}{\partial t} v_1 dx - \int_{\mathcal{R}(\kappa)} (\text{div } \boldsymbol{\sigma}_1) v_1 dx \\ &= \int_{\mathcal{R}(\kappa)} f_1 v_1 dx. \end{aligned} \quad (17)$$

Using integration by parts, we have

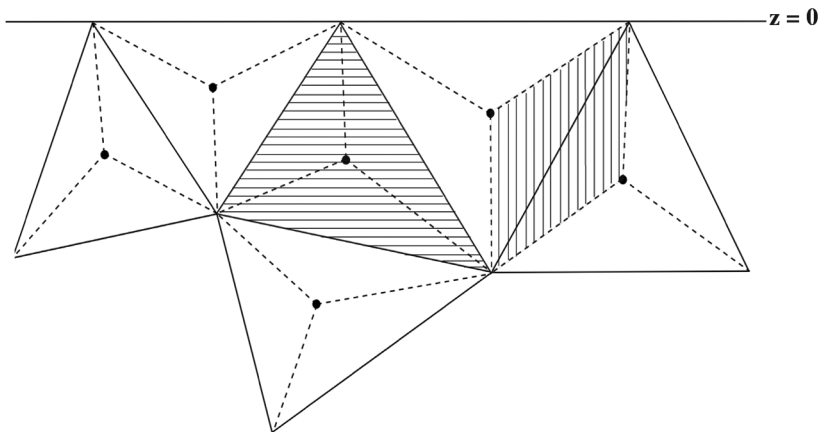


Figure 1. An example of the initial triangulation \mathcal{T}_h' (denoted by solid lines) and the subdivision of triangles of \mathcal{T}_h' by interior points (denoted by solid dots). The newly formed edge in the subdivision process is denoted by dotted lines. The shaded region with horizontal lines is an example of a macroelement $\mathcal{S}(\nu)$, whereas the shaded region with vertical lines is a macroelement $\mathcal{R}(\kappa)$.

$$\begin{aligned} & \int_{\mathcal{R}(\kappa)} \rho \frac{\partial u_1}{\partial t} v_1 dx + \int_{\mathcal{R}(\kappa)} \boldsymbol{\sigma}_1 \cdot \nabla v_1 dx - \int_{\partial \mathcal{R}(\kappa)} (\boldsymbol{\sigma}_1 \cdot \mathbf{n}) v_1 ds \\ &= \int_{\mathcal{R}(\kappa)} f_1 v_1 dx. \end{aligned} \quad (18)$$

Similarly, for the second component of equation 5, we have

$$\begin{aligned} & \int_{\mathcal{R}(\kappa)} \rho \frac{\partial u_2}{\partial t} v_2 dx + \int_{\mathcal{R}(\kappa)} \boldsymbol{\sigma}_2 \cdot \nabla v_2 dx - \int_{\partial \mathcal{R}(\kappa)} (\boldsymbol{\sigma}_2 \cdot \mathbf{n}) v_2 ds \\ &= \int_{\mathcal{R}(\kappa)} f_2 v_2 dx. \end{aligned} \quad (19)$$

Combining the above equations 18 and 19, we have

$$\begin{aligned} & \int_{\mathcal{R}(\kappa)} \rho \frac{\partial \mathbf{u}}{\partial t} \cdot \mathbf{v} dx + \int_{\mathcal{R}(\kappa)} \boldsymbol{\Sigma} \cdot \nabla \mathbf{v} dx - \int_{\partial \mathcal{R}(\kappa)} (\boldsymbol{\Sigma} \mathbf{n}) \cdot \mathbf{v} ds \\ &= \int_{\mathcal{R}(\kappa)} \mathbf{f} \cdot \mathbf{v} dx, \end{aligned} \quad (20)$$

for all smooth test functions $\mathbf{v} = (v_1, v_2)^T$. We remark that equation 20 holds for all macroelements $\mathcal{R}(\kappa)$ and all test functions \mathbf{v} , such that $\mathbf{v} = 0$ on the Dirichlet boundary of the computational domain Ω . We also remark that the above boundary condition for the test function is only applied to the Dirichlet boundary and the boundary where the perfectly matched layer (PML) is used. This boundary condition is not applied to the free surface and periodic boundary.

Next, we consider equation 6. Let $\boldsymbol{\alpha} = (\boldsymbol{\alpha}_1, \boldsymbol{\alpha}_2)^T$ be a smooth 2×2 test tensor, where $\boldsymbol{\alpha}_1$ and $\boldsymbol{\alpha}_2$ are two row vectors. Notice that $\boldsymbol{\alpha}$ is not necessarily symmetric. Multiplying equation 6 by $\boldsymbol{\alpha}$ and integrating on the macroelement $\mathcal{S}(\nu)$, we have

$$\int_{\mathcal{S}(\nu)} \mathbf{A} \frac{\partial \boldsymbol{\Sigma}}{\partial t} \cdot \boldsymbol{\alpha} dx - \int_{\mathcal{S}(\nu)} \nabla \mathbf{u} \cdot \boldsymbol{\alpha} dx + \int_{\mathcal{S}(\nu)} \boldsymbol{\Gamma} \cdot \boldsymbol{\alpha} dx = 0. \quad (21)$$

For the gradient term involving $\boldsymbol{\alpha}_1$, we apply integration by parts to get

$$\int_{\mathcal{S}(\nu)} \nabla u_1 \cdot \boldsymbol{\alpha}_1 dx = - \int_{\mathcal{S}(\nu)} u_1 \operatorname{div} \boldsymbol{\alpha}_1 dx + \int_{\partial \mathcal{S}(\nu)} u_1 (\boldsymbol{\alpha}_1 \cdot \mathbf{n}) ds. \quad (22)$$

Similarly, for the gradient term involving $\boldsymbol{\alpha}_2$, we have

$$\begin{aligned} & \int_{\mathcal{S}(\nu)} \nabla u_2 \cdot \boldsymbol{\alpha}_2 dx \\ &= - \int_{\mathcal{S}(\nu)} u_2 \operatorname{div} \boldsymbol{\alpha}_2 dx + \int_{\partial \mathcal{S}(\nu)} u_2 (\boldsymbol{\alpha}_2 \cdot \mathbf{n}) ds. \end{aligned} \quad (23)$$

Hence, using equations 22 and 23, we have

$$\begin{aligned} & \int_{\mathcal{S}(\nu)} \mathbf{A} \frac{\partial \boldsymbol{\Sigma}}{\partial t} \cdot \boldsymbol{\alpha} dx + \int_{\mathcal{S}(\nu)} \mathbf{u} \operatorname{div} \boldsymbol{\alpha} dx - \int_{\partial \mathcal{S}(\nu)} \mathbf{u} \cdot (\boldsymbol{\alpha} \mathbf{n}) ds \\ &+ \int_{\mathcal{S}(\nu)} \boldsymbol{\Gamma} \cdot \boldsymbol{\alpha} dx = 0. \end{aligned} \quad (24)$$

Now, we will present the definition of the SDG method. The approximations of \mathbf{u} , $\boldsymbol{\Sigma}$, and $\boldsymbol{\Gamma}$ are denoted by \mathbf{u}_h , $\boldsymbol{\Sigma}_h$, and $\boldsymbol{\Gamma}_h$ and are obtained in the spaces $(U_h)^2$, $(W_h)^2$ and X_h , respectively. For any macroelement $\mathcal{R}(\kappa)$, equation 20 suggests the following approximation:

$$\begin{aligned} & \int_{\mathcal{R}(\kappa)} \rho \frac{\partial \mathbf{u}_h}{\partial t} \cdot \mathbf{v} dx + \int_{\mathcal{R}(\kappa)} \boldsymbol{\Sigma}_h \cdot \nabla \mathbf{v} dx - \int_{\partial \mathcal{R}(\kappa)} (\boldsymbol{\Sigma}_h \mathbf{n}) \cdot \mathbf{v} ds \\ &= \int_{\mathcal{R}(\kappa)} \mathbf{f} \cdot \mathbf{v} dx, \end{aligned} \quad (25)$$

for any test function \mathbf{v} in the space $(U_h)^2$. Summing over all $\mathcal{R}(\kappa)$, we have

$$\begin{aligned} & \int_{\Omega} \rho \frac{\partial \mathbf{u}_h}{\partial t} \cdot \mathbf{v} dx + \sum_{\kappa \in \mathcal{F}_u} \left(\int_{\mathcal{R}(\kappa)} \boldsymbol{\Sigma}_h \cdot \nabla \mathbf{v} dx - \int_{\partial \mathcal{R}(\kappa)} (\boldsymbol{\Sigma}_h \mathbf{n}) \cdot \mathbf{v} ds \right) \\ &= \int_{\Omega} \mathbf{f} \cdot \mathbf{v} dx, \quad \forall \mathbf{v} \in (U_h)^2. \end{aligned} \quad (26)$$

For any macroelement $\mathcal{S}(\nu)$, equation 24 suggests the following approximation:

$$\begin{aligned} & \int_{\mathcal{S}(\nu)} \mathbf{A} \frac{\partial \boldsymbol{\Sigma}_h}{\partial t} \cdot \boldsymbol{\alpha} dx + \int_{\mathcal{S}(\nu)} \mathbf{u}_h \operatorname{div} \boldsymbol{\alpha} dx \\ &- \int_{\partial \mathcal{S}(\nu)} \mathbf{u}_h \cdot (\boldsymbol{\alpha} \mathbf{n}) ds + \int_{\mathcal{S}(\nu)} \boldsymbol{\Gamma}_h \cdot \boldsymbol{\alpha} dx = 0, \end{aligned} \quad (27)$$

for any test function $\boldsymbol{\alpha}$ in the space $(W_h)^2$. Summing over all $\mathcal{S}(\nu)$, we have

$$\begin{aligned} & \int_{\Omega} \mathbf{A} \frac{\partial \boldsymbol{\Sigma}_h}{\partial t} \cdot \boldsymbol{\alpha} dx + \sum_{\nu \in \mathcal{N}} \left(\int_{\mathcal{S}(\nu)} \mathbf{u}_h \operatorname{div} \boldsymbol{\alpha} dx - \int_{\partial \mathcal{S}(\nu)} \mathbf{u}_h \cdot (\boldsymbol{\alpha} \mathbf{n}) ds \right) \\ &+ \int_{\Omega} \boldsymbol{\Gamma}_h \cdot \boldsymbol{\alpha} dx = 0, \quad \forall \boldsymbol{\alpha} \in (W_h)^2. \end{aligned} \quad (28)$$

In addition, we will impose the following weak symmetry condition for $\boldsymbol{\Sigma}_h$

$$\int_{\Omega} \boldsymbol{\Sigma}_h \cdot \boldsymbol{\eta} dx = 0, \quad \forall \boldsymbol{\eta} \in X_h. \quad (29)$$

Equations 26, 28, and 29 give the definition of our SDG method. Throughout the paper, we write $\mathbf{u}_h = (\mathbf{u}_{h,1}, \mathbf{u}_{h,2})^T$ and $\boldsymbol{\Sigma}_h = (\boldsymbol{\sigma}_{h,1}, \boldsymbol{\sigma}_{h,2})^T$, where $\boldsymbol{\sigma}_{h,i}$ is the i th row of $\boldsymbol{\Sigma}_h$.

Next, we will derive the linear system arising from equations 26, 28, and 29. Assume that the dimensions of U_h , W_h , and X_h are m_U , m_W , and m_X , respectively. Let $\{v^{(i)}\}_{i=1}^{m_U}$ be the basis functions of U_h , $\{\boldsymbol{\alpha}^{(i)}\}_{i=1}^{m_W}$ be the basis functions of W_h , and $\{\boldsymbol{\eta}^{(i)}\}_{i=1}^{m_X}$ be the basis functions of X_h . Each component of \mathbf{u}_h can be represented by

$$\mathbf{u}_{h,k} = \sum_{i=1}^{m_U} u_{h,k}^{(i)} v^{(i)}, \quad k = 1, 2. \quad (30)$$

Moreover, each row of $\Sigma_{\mathbf{h}}$ can be represented by

$$\sigma_{\mathbf{h},k} = \sum_{i=1}^{m_W} \sigma_{h,k}^{(i)} \alpha^{(i)}, \quad k = 1, 2. \quad (31)$$

Similarly, $\Gamma_{\mathbf{h}}$ can be represented by

$$\Gamma_{\mathbf{h}} = \sum_{i=1}^{m_X} \gamma_h^{(i)} \eta^{(i)}. \quad (32)$$

We define the $m_U \times m_U$ mass matrix \mathbf{M}_u by

$$(\mathbf{M}_u)_{ij} = \int_{\Omega} \rho v^{(i)} v^{(j)} dx. \quad (33)$$

Notice that the basis functions of $(W_h)^2$ have the form $\beta^{(i)} = (\alpha^{(i)}, 0)^T$ or $\beta^{(i)} = (0, \alpha^{(i)})^T$. Thus, we define the $2m_W \times 2m_W$ mass matrix \mathbf{M}_{σ} by

$$(\mathbf{M}_{\sigma})_{ij} = \int_{\Omega} (\mathbf{A}\beta^{(i)}) \cdot \beta^{(j)} dx. \quad (34)$$

We also define the $2m_W \times m_X$ matrix \mathbf{C}_{γ} by

$$(\mathbf{C}_{\gamma})_{ij} = \int_{\Omega} \beta^{(i)} \cdot \eta^{(j)} dx. \quad (35)$$

Moreover, with $v^{(i)} \in U_h$ and $\alpha^{(j)} \in W_h$, we define the following $m_U \times m_W$ matrix \mathbf{B} by

$$\mathbf{B}_{ij} = \sum_{\kappa \in \mathcal{F}_u} \left(\int_{\mathcal{R}(\kappa)} \alpha^{(j)} \cdot \nabla v^{(i)} dx - \int_{\partial \mathcal{R}(\kappa)} (\alpha^{(j)} \cdot \mathbf{n}) v^{(i)} ds \right), \quad (36)$$

and the following $m_W \times m_U$ matrix \mathbf{B}^* by

$$\mathbf{B}_{ji}^* = - \sum_{\nu \in \mathcal{N}} \left(\int_{\mathcal{S}(\nu)} \mathbf{v}^{(i)} \operatorname{div} \alpha^{(j)} dx - \int_{\partial \mathcal{S}(\nu)} \mathbf{v}^{(i)} (\alpha^{(j)} \cdot \mathbf{n}) ds \right). \quad (37)$$

Finally, we define the following two $m_U \times 1$ vectors $\vec{\mathbf{f}}_k = (f_k^{(i)})$ by

$$f_k^{(i)} = \int_{\Omega} f_k v^{(i)} dx, \quad k = 1, 2. \quad (38)$$

Let $\vec{\mathbf{u}}_1 = (u_{h,1}^{(i)})$ and $\vec{\mathbf{u}}_2 = (u_{h,2}^{(i)})$ be vectors of coefficients giving the approximate solutions $u_{h,1}$ and $u_{h,2}$ in equation 30. Moreover, we let $\vec{\sigma}_1 = (\sigma_{h,1}^{(i)})$ and $\vec{\sigma}_2 = (\sigma_{h,2}^{(i)})$ be vectors of coefficients giving the approximate solutions $\sigma_{h,1}$ and $\sigma_{h,2}$ in equation 31. We write $\vec{\sigma} = (\vec{\sigma}_1, \vec{\sigma}_2)^T$. Finally, we let $\vec{\gamma} = (\gamma_h^{(i)})$ be the vector of coefficients giving the approximate solutions $\Gamma_{\mathbf{h}}$ in equation 32. Using these definitions, equation 26 can be written as

$$\frac{d}{dt} \mathbf{M}_u \vec{\mathbf{u}}_1 + \mathbf{B} \vec{\sigma}_1 = \vec{\mathbf{f}}_1, \quad \frac{d}{dt} \mathbf{M}_u \vec{\mathbf{u}}_2 + \mathbf{B} \vec{\sigma}_2 = \vec{\mathbf{f}}_2. \quad (39)$$

Moreover, equation 26 can be written as

$$\frac{d}{dt} (\mathbf{M}_{\sigma} \vec{\sigma}) - \begin{pmatrix} \mathbf{B}^* & 0 \\ 0 & \mathbf{B}^* \end{pmatrix} \begin{pmatrix} \vec{\mathbf{u}}_1 \\ \vec{\mathbf{u}}_2 \end{pmatrix} + \mathbf{C}_{\gamma} \vec{\gamma} = 0. \quad (40)$$

Finally, equation 29 can be written as

$$\mathbf{C}_{\gamma}^T \vec{\sigma} = 0. \quad (41)$$

Equations 39, 40, and 41 define the linear system for the SDG method. We remark that matrix \mathbf{B}^* is the transpose of the matrix \mathbf{B} , which is proved in Chung and Engquist (2009). We also remark that the convergence of our method can be proved using techniques in Chung and Engquist (2009) and Stenberg (1988).

Time discretization

For time discretization, we will apply the standard ‘‘leap-frog’’ scheme. The velocity field $\vec{\mathbf{u}}$ is computed at the times $t_n = n\Delta t$, whereas the stress tensors $\vec{\Sigma}$ and $\vec{\gamma}$ are computed at $t_{n+\frac{1}{2}} = (n + \frac{1}{2})\Delta t$, where Δt is the time step size and n is a nonnegative integer. We will use $\vec{\mathbf{u}}^n$ to denote the approximate value of $\vec{\mathbf{u}}$ at time t_n . Moreover, we will use $\vec{\Sigma}^{n+\frac{1}{2}}$ and $\vec{\gamma}^{n+\frac{1}{2}}$ to denote the approximate values of $\vec{\Sigma}$ and $\vec{\gamma}$ at time $t_{n+\frac{1}{2}}$, respectively.

For equation 39, we use the central difference approximation in time at $t_{n+\frac{1}{2}}$ to obtain the following approximation:

$$\begin{aligned} \mathbf{M}_u \frac{\vec{\mathbf{u}}_1^{n+1} - \vec{\mathbf{u}}_1^n}{\Delta t} + \mathbf{B} \vec{\sigma}_1^{n+\frac{1}{2}} &= \vec{\mathbf{f}}_1^{n+\frac{1}{2}}, \\ \mathbf{M}_u \frac{\vec{\mathbf{u}}_2^{n+1} - \vec{\mathbf{u}}_2^n}{\Delta t} + \mathbf{B} \vec{\sigma}_2^{n+\frac{1}{2}} &= \vec{\mathbf{f}}_2^{n+\frac{1}{2}}. \end{aligned} \quad (42)$$

On the other hand, we evaluate equations 40 and 41 at the time t_n and use the central difference approximation for the time derivative to obtain the following:

$$\begin{aligned} \mathbf{M}_{\sigma} \frac{\vec{\sigma}^{n+\frac{3}{2}} - \vec{\sigma}^{n+\frac{1}{2}}}{\Delta t} - \tilde{\mathbf{B}}^* \vec{\mathbf{u}}^{n+1} + \mathbf{C}_{\gamma} \frac{\vec{\gamma}^{n+\frac{3}{2}} + \vec{\gamma}^{n+\frac{1}{2}}}{2} &= 0, \\ \mathbf{C}_{\gamma}^T \vec{\sigma}^{n+\frac{3}{2}} &= 0, \end{aligned} \quad (43)$$

where

$$\tilde{\mathbf{B}}^* = \begin{pmatrix} \mathbf{B}^* & 0 \\ 0 & \mathbf{B}^* \end{pmatrix}. \quad (44)$$

Equation 43 can be written as the following saddle point system:

$$\begin{aligned} \frac{2}{\Delta t} \mathbf{M}_{\sigma} \vec{\Sigma}^{n+\frac{3}{2}} + \mathbf{C}_{\gamma} \vec{\gamma}^{n+\frac{3}{2}} - \frac{2}{\Delta t} \mathbf{M}_{\sigma} \vec{\sigma}^{n+\frac{1}{2}} - \mathbf{C}_{\gamma} \vec{\gamma}^{n+\frac{1}{2}} + 2\tilde{\mathbf{B}}^* \vec{\mathbf{u}}^{n+1} &:= \vec{\mathbf{r}}^{n+\frac{1}{2}}, \\ \mathbf{C}_{\gamma}^T \vec{\sigma}^{n+\frac{3}{2}} &= 0. \end{aligned} \quad (45)$$

Equations 42 and 45 define the time-marching formula. In particular, for any given $\vec{\mathbf{u}}^n$, $\vec{\sigma}^{n+\frac{1}{2}}$, and $\vec{\gamma}^{n+\frac{1}{2}}$, where $n = 0, 1, 2, \dots$, we can use equation 42 to obtain $\vec{\mathbf{u}}^{n+1}$. Then, using the newly obtained

$\bar{\mathbf{u}}^{n+1}$, and current values of $\bar{\boldsymbol{\sigma}}^{n+\frac{1}{2}}$ and $\bar{\boldsymbol{\gamma}}^{n+\frac{1}{2}}$, we can use equation 45 to obtain approximations $\bar{\boldsymbol{\sigma}}^{n+\frac{3}{2}}$ and $\bar{\boldsymbol{\gamma}}^{n+\frac{3}{2}}$.

Although equation 45 is a coupled system with respect to the unknowns $\bar{\boldsymbol{\sigma}}^{n+\frac{3}{2}}$ and $\bar{\boldsymbol{\gamma}}^{n+\frac{3}{2}}$, it can be solved in the following element-wise manner: Because the mass matrix \mathbf{M}_σ and the matrix \mathbf{C}_γ are block diagonal, namely

$$\mathbf{M}_\sigma = \begin{pmatrix} \mathbf{M}_\sigma^{S(\nu_1)} & & & \\ & \mathbf{M}_\sigma^{S(\nu_2)} & & \\ & & \ddots & \\ & & & \mathbf{M}_\sigma^{S(\nu_N)} \end{pmatrix}$$

and $\mathbf{C}_\gamma = \begin{pmatrix} \mathbf{C}_\gamma^{S(\nu_1)} & & & \\ & \mathbf{C}_\gamma^{S(\nu_2)} & & \\ & & \ddots & \\ & & & \mathbf{C}_\gamma^{S(\nu_N)} \end{pmatrix}$, (46)

where N is the number of triangles in the initial triangulation \mathcal{T}_h' , $\mathbf{M}_\sigma^{S(\nu_i)}$ is the local mass matrix corresponding to the macroelement $S(\nu_i)$, and $\mathbf{C}_\gamma^{S(\nu_i)}$ is the restriction of \mathbf{C}_γ to the components corresponding to the macroelement $S(\nu_i)$, equation 45 can be solved as

$$\frac{2}{\Delta t} \mathbf{M}_\sigma^{S(\nu_i)} \bar{\boldsymbol{\sigma}}^{n+\frac{3}{2}} + \mathbf{C}_\gamma^{S(\nu_i)} \bar{\boldsymbol{\gamma}}^{n+\frac{3}{2}} = \bar{\mathbf{r}}^{n+\frac{1}{2}},$$

$$(\mathbf{C}_\gamma^{S(\nu_i)})^T \bar{\boldsymbol{\sigma}}^{n+\frac{3}{2}} = 0, \quad (47)$$

where $\bar{\boldsymbol{\sigma}}^{n+\frac{3}{2}}$, $\bar{\boldsymbol{\gamma}}^{n+\frac{3}{2}}$, and $\bar{\mathbf{r}}^{n+\frac{1}{2}}$ are understood as the restriction to the components corresponding to the macroelement $S(\nu_i)$. Similarly, the mass matrix \mathbf{M}_u is also block diagonal, namely,

$$\mathbf{M}_u = \begin{pmatrix} \mathbf{M}_u^{\mathcal{R}(\kappa_1)} & & & \\ & \mathbf{M}_u^{\mathcal{R}(\kappa_2)} & & \\ & & \ddots & \\ & & & \mathbf{M}_u^{\mathcal{R}(\kappa_F)} \end{pmatrix}, \quad (48)$$

where F is the number of second-type macroelements, which is the same as the number of edges in the initial triangulation \mathcal{T}_h' . Therefore, equation 42 can be solved element-by-element as well.

The system defined in equation 47 is invertible. From the classical theory of saddle point problem, we need to show that, for every $\eta \in X_h$, there exists $\alpha \in (W_h)^2$, such that

$$\int_\Omega (\alpha_{12} - \alpha_{21}) \eta dx := \int_\Omega \boldsymbol{\alpha} \cdot \boldsymbol{\eta} dx = \int_\Omega \eta^2 dx, \quad (49)$$

and

$$\int_\Omega \mathbf{A} \boldsymbol{\alpha} \cdot \boldsymbol{\alpha} dx \leq K_0 \int_\Omega \eta^2 dx, \quad (50)$$

where α_{12} is the second component of $\alpha_1 \in W_h$, α_{21} is the first component of $\alpha_2 \in W_h$, and $K_0 > 0$ is a constant independent of the mesh size. Consider a triangle $\tau \in \mathcal{T}_h$. From the theory of Chung and Engquist (2009), we can find a unique α_1 satisfying

$$\alpha_1 \cdot \mathbf{n} = 0, \quad \text{on } \kappa \in \partial\tau \cap \mathcal{F}_\sigma,$$

$$\int_\tau \alpha_{11} \eta dx = 0,$$

$$\int_\tau \alpha_{11} \eta dx = \frac{1}{2} \int_\tau \eta^2 dx. \quad (51)$$

Similarly, we can find a unique α_2 satisfying

$$\alpha_2 \cdot \mathbf{n} = 0, \quad \text{on } \kappa \in \partial\tau \cap \mathcal{F}_\sigma,$$

$$\int_\tau \alpha_{21} \eta dx = -\frac{1}{2} \int_\tau \eta^2 dx,$$

$$\int_\tau \alpha_{22} \eta dx = 0. \quad (52)$$

Note that the above constructions can be done on each $\tau \in \mathcal{T}_h$ without destroying the continuity conditions in the space W_h . Finally, from the above construction, we can see easily that equations 46 and 47 hold.

Numerical stability

We will now derive a sufficient condition on the size of Δt for the stability of the SDG method in equations 42 and 43. We will assume that the source term $\mathbf{f} = 0$ to simplify the calculations, and we remark that the same steps can be used to show stability of the method when $\mathbf{f} \neq 0$. First, multiplying equation 43 by $\bar{\mathbf{u}}^{n+1} + \bar{\mathbf{u}}^n$, we obtain for $k = 1$ and 2

$$\left(\mathbf{M}_u \frac{\bar{\mathbf{u}}_k^{n+1} - \bar{\mathbf{u}}_k^n}{\Delta t}, \bar{\mathbf{u}}_k^{n+1} + \bar{\mathbf{u}}_k^n \right) + \left(\mathbf{B} \bar{\boldsymbol{\sigma}}_k^{n+\frac{1}{2}}, \bar{\mathbf{u}}_k^{n+1} + \bar{\mathbf{u}}_k^n \right)$$

$$= \left(\mathbf{f}_k^{n+\frac{1}{2}}, \bar{\mathbf{u}}_k^{n+1} + \bar{\mathbf{u}}_k^n \right). \quad (53)$$

Moreover, multiplying equation 43 by $\bar{\boldsymbol{\sigma}}^{n+\frac{3}{2}} + \bar{\boldsymbol{\sigma}}^{n+\frac{1}{2}}$, we obtain

$$\left(\mathbf{M}_\sigma \frac{\bar{\boldsymbol{\sigma}}^{n+\frac{3}{2}} - \bar{\boldsymbol{\sigma}}^{n+\frac{1}{2}}}{\Delta t}, \bar{\boldsymbol{\sigma}}^{n+\frac{3}{2}} + \bar{\boldsymbol{\sigma}}^{n+\frac{1}{2}} \right)$$

$$- \left(\tilde{\mathbf{B}}^* \bar{\mathbf{u}}^{n+1}, \bar{\boldsymbol{\sigma}}^{n+\frac{3}{2}} + \bar{\boldsymbol{\sigma}}^{n+\frac{1}{2}} \right) = 0. \quad (54)$$

By the fact that $\mathbf{B}^* = \mathbf{B}^T$, which is proved by Chung and Engquist (2009) and the definition of $\tilde{\mathbf{B}}^*$, we have

$$\left(\mathbf{B} \bar{\boldsymbol{\sigma}}_1^{n+\frac{1}{2}}, \bar{\mathbf{u}}_1^n \right) + \left(\mathbf{B} \bar{\boldsymbol{\sigma}}_2^{n+\frac{1}{2}}, \bar{\mathbf{u}}_2^n \right) - \left(\tilde{\mathbf{B}}^* \bar{\mathbf{u}}^n, \bar{\boldsymbol{\sigma}}^{n+\frac{1}{2}} \right)$$

$$= \left(\bar{\boldsymbol{\sigma}}_1^{n+\frac{1}{2}}, \mathbf{B}^T \bar{\mathbf{u}}_1^n \right) + \left(\bar{\boldsymbol{\sigma}}_2^{n+\frac{1}{2}}, \mathbf{B}^T \bar{\mathbf{u}}_2^n \right) - \left(\tilde{\mathbf{B}}^* \bar{\mathbf{u}}^n, \bar{\boldsymbol{\sigma}}^{n+\frac{1}{2}} \right),$$

$$= \left(\bar{\boldsymbol{\sigma}}_1^{n+\frac{1}{2}}, \mathbf{B}^* \bar{\mathbf{u}}_1^n \right) + \left(\bar{\boldsymbol{\sigma}}_2^{n+\frac{1}{2}}, \mathbf{B}^* \bar{\mathbf{u}}_2^n \right) - \left(\tilde{\mathbf{B}}^* \bar{\mathbf{u}}^n, \bar{\boldsymbol{\sigma}}^{n+\frac{1}{2}} \right),$$

$$= 0. \quad (55)$$

Let $N > 1$ be a fixed integer. Summing equations 53 and 54 from $n = 0$ to $n = N - 1$ and using equation 55, we have

$$E^N = E^0 + \frac{\Delta t}{2} \left(\tilde{\mathbf{B}} \tilde{\boldsymbol{\sigma}}^{N+\frac{1}{2}}, \tilde{\mathbf{u}}^N \right) - \frac{\Delta t}{2} \left(\tilde{\boldsymbol{\sigma}}^{\frac{1}{2}}, \tilde{\mathbf{B}}^* \tilde{\mathbf{u}}^0 \right), \quad (56)$$

where

$$E^n := \frac{1}{2} \left(\|\tilde{\mathbf{u}}_1^n\|_{\mathbf{M}_u}^2 + \|\tilde{\mathbf{u}}_2^n\|_{\mathbf{M}_u}^2 + \|\tilde{\boldsymbol{\sigma}}^{n+\frac{1}{2}}\|_{\mathbf{M}_\sigma}^2 \right), \quad (57)$$

and the norms above are defined as

$$\|\tilde{\mathbf{u}}_k^n\|_{\mathbf{M}_u}^2 = (\mathbf{M}_u \tilde{\mathbf{u}}_k^n, \tilde{\mathbf{u}}_k^n), \quad k=1,2; \quad \|\tilde{\boldsymbol{\sigma}}^{n+\frac{1}{2}}\|_{\mathbf{M}_\sigma}^2 = (\mathbf{M}_\sigma \tilde{\boldsymbol{\sigma}}^{n+\frac{1}{2}}, \tilde{\boldsymbol{\sigma}}^{n+\frac{1}{2}}). \quad (58)$$

Let $\mathbf{K} := \tilde{\mathbf{M}}_u^{-\frac{1}{2}} \tilde{\mathbf{B}} \mathbf{M}_\sigma^{-\frac{1}{2}}$, where

$$\tilde{\mathbf{M}}_u = \begin{pmatrix} \mathbf{M}_u & 0 \\ 0 & \mathbf{M}_u \end{pmatrix}. \quad (59)$$

By the Cauchy-Schwarz inequality, we have

$$\left(\tilde{\mathbf{B}} \tilde{\boldsymbol{\sigma}}^{N+\frac{1}{2}}, \tilde{\mathbf{u}}^N \right) \leq \|\mathbf{K}\|_2 \|\tilde{\mathbf{u}}^N\|_{\tilde{\mathbf{M}}_u} \|\tilde{\boldsymbol{\sigma}}^{N+\frac{1}{2}}\|_{\mathbf{M}_\sigma}, \quad (60)$$

where

$$\|\tilde{\mathbf{u}}^N\|_{\tilde{\mathbf{M}}_u}^2 = \|\tilde{\mathbf{u}}_1^N\|_{\mathbf{M}_u}^2 + \|\tilde{\mathbf{u}}_2^N\|_{\mathbf{M}_u}^2. \quad (61)$$

We will now show that the SDG method is stable if $\Lambda := \Delta t \|\mathbf{K}\|_2 < 2$. Using this assumption, equation 56 can be written as

$$E^N \leq E^0 + \frac{\Lambda}{2} \|\tilde{\mathbf{u}}^N\|_{\tilde{\mathbf{M}}_u} \|\tilde{\boldsymbol{\sigma}}^{N+\frac{1}{2}}\|_{\mathbf{M}_\sigma} + \frac{\Lambda}{2} \|\tilde{\mathbf{u}}^0\|_{\tilde{\mathbf{M}}_u} \|\tilde{\boldsymbol{\sigma}}^{\frac{1}{2}}\|_{\mathbf{M}_\sigma}, \quad (62)$$

which becomes

$$E^N \leq E^0 + \frac{\Lambda}{4} \left(\|\tilde{\mathbf{u}}^N\|_{\tilde{\mathbf{M}}_u}^2 + \|\tilde{\boldsymbol{\sigma}}^{N+\frac{1}{2}}\|_{\mathbf{M}_\sigma}^2 \right) + \frac{\Lambda}{4} \left(\|\tilde{\mathbf{u}}^0\|_{\tilde{\mathbf{M}}_u}^2 + \|\tilde{\boldsymbol{\sigma}}^{\frac{1}{2}}\|_{\mathbf{M}_\sigma}^2 \right). \quad (63)$$

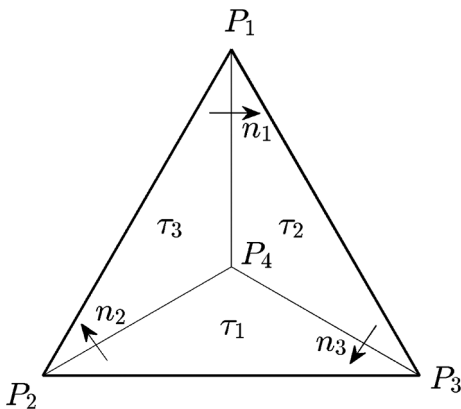


Figure 2. Notations for the construction of basis for W_h .

Hence, we have

$$E^N \leq \frac{1 + \frac{\Lambda}{2}}{1 - \frac{\Lambda}{2}} E^0, \quad (64)$$

provided $1 - \Lambda/2 > 0$. The above inequality gives the stability of the SDG method because $\Lambda < 2$. To find the explicit form of $\|\mathbf{K}\|_2$, it is known that $\|\mathbf{K}\|_2$ is proportional to h^{-1} , where h is the mesh size because the operator \mathbf{K} is a discrete first-order derivative operator. Thus, we can write

$$\|\mathbf{K}\|_2 = Ch^{-1}, \quad (65)$$

for some constant C . The value of C can be found by computing $\|\mathbf{K}\|_2$ for different values of h and by using a least-squares fitting.

Construction of basis functions

We will present the construction of basis functions in this section. First, we describe the basis functions for U_h . By definition, a function $v \in U_h$ is a polynomial of degree $m \geq 1$ on each triangle $\tau \in \mathcal{T}_h$ and is continuous on the edges $\kappa \in \mathcal{F}_u^0$. Thus, v is decoupled along the boundaries of the second-type macroelement $\mathcal{R}(\kappa)$ for all $\kappa \in \mathcal{F}_u$. Therefore, the basis functions for the space U_h are constructed locally on $\mathcal{R}(\kappa)$. We will consider an interior edge $\kappa \in \mathcal{F}_u^0$ and discuss the corresponding construction of basis functions on $\mathcal{R}(\kappa)$. The case that κ belongs to the boundary of the computational domain can be constructed in the same way. With reference to Figure 1, we will need piecewise polynomials of degree m that are continuous on κ . Thus, the basis functions can be taken as the standard conforming finite-element basis functions applied to the domain $\mathcal{R}(\kappa)$ with a triangulation composed of two triangles. Second, for the space X_h , the basis functions can be taken as Lagrange basis functions on each triangle in \mathcal{T}_h because there is no continuity requirement.

Finally, we describe the construction of the basis functions for the space W_h . By definition, a vector $\alpha \in W_h$ is a vector polynomial on each triangle $\tau \in \mathcal{T}_h$ with continuous normal components on the edges $\kappa \in \mathcal{F}_\sigma$. Thus, α is decoupled along the boundaries of the first-type macroelements $\mathcal{S}(\nu)$ for all $\nu \in \mathcal{N}$. Therefore, the basis functions for the space W_h are constructed locally on $\mathcal{S}(\nu)$. We will now present a convenient way to construct these functions. Consider a first-type macroelement $\mathcal{S}(\nu)$. Let P_1, P_2 , and P_3 be the three vertices of $\mathcal{S}(\nu)$ and $P_4 = \nu$, which is the point chosen for the subdivision process required by the SDG method (see Figure 2). The corresponding three subtriangles are denoted by $\tau_1 = P_2P_3P_4$, $\tau_2 = P_1P_3P_4$, and $\tau_3 = P_1P_2P_4$. Moreover, for each of the three edges P_kP_4 ($k=1,2,3$), in the interior of $\mathcal{S}(\nu)$, we define a region ω_k by the union of the two subtriangles having the edge P_kP_4 . That is, $\omega_1 = \tau_2 \cup \tau_3$, $\omega_2 = \tau_1 \cup \tau_3$, and $\omega_3 = \tau_1 \cup \tau_2$. In addition, we use \mathbf{n}_k , $k=1,2,3$, to denote a fixed unit normal vector for the edges P_kP_4 . The basis functions are divided into three types, and each of these three types of basis functions is supported in ω_1, ω_2 , and ω_3 , respectively. We will present the construction of basis function for the first type, namely, those basis functions having support in ω_1 . The other two types can be constructed similarly. For the first type of basis functions α , we impose the following conditions:

$$\alpha \cdot \mathbf{n}_2 = 0, \quad \text{on } P_2P_4; \quad \alpha \cdot \mathbf{n}_3 = 0, \quad \text{on } P_3P_4, \quad (66)$$

that is, α has a zero normal component on the edges P_2P_4 and P_3P_4 . To obtain the above condition, we require $\alpha \cdot \mathbf{n}_2$ to be identically zero on ω_2 and $\alpha \cdot \mathbf{n}_3$ to be identically zero on ω_3 . Notice that, using this construction, we have $\alpha \cdot \mathbf{n}_2$ and $\alpha \cdot \mathbf{n}_3$ are identically zero on τ_1 because τ_1 is the intersection of ω_2 and ω_3 . Next, we recall that the space W_h requires that $\alpha \cdot \mathbf{n}_1$ be continuous on P_1P_4 . We now consider ω_1 and define $\alpha \cdot \mathbf{n}_1$ to be a polynomial of degree m in each subtriangle of ω_1 , such that $\alpha \cdot \mathbf{n}_1$ is continuous on P_1P_4 . Similar to the construction of basis functions for the space U_h , we now choose basis functions of $\alpha \cdot \mathbf{n}_1$ on ω_1 to be the classical conforming finite-element basis functions defined in the domain ω_1 corresponding to the triangulation $\omega_1 = \tau_2 \cup \tau_3$. The construction of basis function is now completed. Because $\alpha \cdot \mathbf{n}_1$ and $\alpha \cdot \mathbf{n}_3$ are specified in τ_2 , the vector α in τ_2 can be reconstructed. Similarly, $\alpha \cdot \mathbf{n}_1$ and $\alpha \cdot \mathbf{n}_2$ are specified in τ_3 , so that the vector α can be reconstructed. Specifically, we can then write

$$\alpha(x) \cdot \mathbf{n}_1 = \begin{cases} g_2(x) & \text{in } \tau_2, \\ g_3(x) & \text{in } \tau_3, \end{cases} \quad (67)$$

where g_2 and g_3 are polynomials of degree m chosen in the way explained above. On τ_2 , we have $\alpha \cdot \mathbf{n}_1 = g_2$ and $\alpha \cdot \mathbf{n}_3 = 0$. Hence, we have on τ_2

$$\alpha = \frac{g_2}{1 - (\mathbf{n}_1 \cdot \mathbf{n}_3)^2} \mathbf{n}_1 - \frac{(\mathbf{n}_1 \cdot \mathbf{n}_3)g_2}{1 - (\mathbf{n}_1 \cdot \mathbf{n}_3)^2} \mathbf{n}_3. \quad (68)$$

Similarly, we have on τ_3

$$\alpha = \frac{g_3}{1 - (\mathbf{n}_1 \cdot \mathbf{n}_2)^2} \mathbf{n}_1 - \frac{(\mathbf{n}_1 \cdot \mathbf{n}_2)g_3}{1 - (\mathbf{n}_1 \cdot \mathbf{n}_2)^2} \mathbf{n}_2. \quad (69)$$

In Figure 3, plots of the first type of basis functions for the case $m = 1$ are shown. Notice that, these basis functions have support in ω_1 . Moreover because $m = 1$, there are only four distinct basis functions. In particular, ω_1 is the union of two subtriangles τ_2 and τ_3 . By the above construction, we need basis functions for $\alpha \cdot \mathbf{n}_1$ that are linear in each of τ_2 and τ_3 , and are continuous on P_1P_4 . Thus, we see that there are only four choices, by taking $\alpha \cdot \mathbf{n}_1$ equal to one at one of the four vertices of ω_1 and zero at the other three vertices.

NUMERICAL RESULTS

In this section, we present some numerical results to show the performance of the SDG method for the simulation of seismic waves. In our test examples, the velocities and stresses are zero initially, and a point source is vertically excited near the free surface. The source function is taken as the first derivative of a Gaussian function defined as

$$w(t) = 2\pi f_0(t - t_0)e^{-\pi^2 f_0^2(t-t_0)^2}, \quad (70)$$

where f_0 is the frequency (in hertz), and t_0 is a shift in time (in seconds). More precisely, in equation 6, we set $f_1 = 0$ and f_2 to be a point source with the time component being the first derivative of $w(t)$. In all examples shown below, the frequency f_0 is 50 Hz and t_0 is 24 ms.

We will perform computations in rectangular and irregular domains. For rectangular domains, we first subdivide the domain into

equal-size squares, and then we divide each square into two triangles, which forms the initial mesh \mathcal{T}_h' . Then, we choose the centroid as ν in each triangle and subdivide each triangle into three in the way presented in the previous section. The resulting triangulation is \mathcal{T}_h . For computational domains with surface topography, we will use an unstructured mesh as the initial mesh \mathcal{T}_h' near the free surface and use a structured mesh, similar to the one used for rectangular computational domains, as the initial mesh \mathcal{T}_h' for the rest of the computational domain (see Figure 4 for an illustration). The purpose of doing this is to make the simulations more efficient. We remark that the diameter of the triangles in the unstructured mesh is

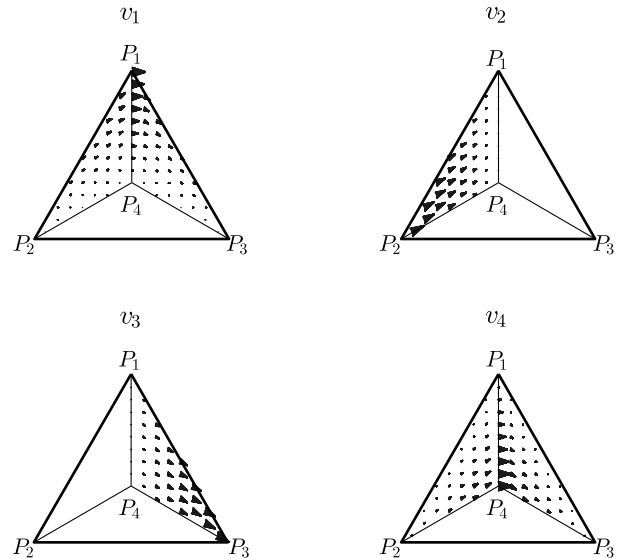


Figure 3. Plots of the first-type basis functions for W_h on $S(\nu)$ with $m = 1$.

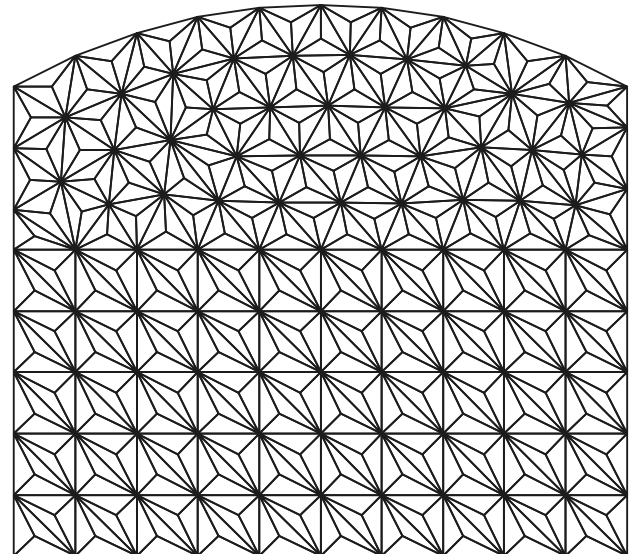


Figure 4. A schematic for an initial triangulation for computational domains with surface topography, where unstructured mesh is used near the free surface and regular mesh is used for the rest of the domain.

about the same size as the diameters of the triangles in the regular mesh. In all simulations, we will use $\Delta t \approx 2hC^{-1}$, which is sufficient for stability, where the constant C is determined by equation 65.

For our numerical tests presented below, we will consider the use of four different materials. Their P-wave velocity V_P , S-wave velocity V_S , density ρ , and Poisson's ratio ν are summarized in Table 1.

We can then find a time step Δt to ensure the stability with the method described in the previous section. For example, we obtain $C \approx 8900$ and $C \approx 9130$ for materials 1 and 2, respectively. Thus, the stability conditions for these two cases are $\Delta t < 2.25 \times 10^{-4}h$ and $\Delta t < 2.20 \times 10^{-4}h$, respectively. We remark that this implies that the Courant-Friedrichs-Lewy (CFL) number, defined as $v_p \Delta t/h$ is approximately 0.117. We recall that the CFL number for the second-order FDM is approximately 0.707. Hence, the stability condition for our SDG method with piecewise linear elements is approximately six times more restrictive than that of the second-order FDM. Notice that this fact is partly due to the regularity of the triangles.

In our first example, called example 1, we will perform the simulations of seismic waves for a point source located near a flat surface without the use of PMLs. The domain of interest is $[40, 240 \text{ m}] \times [0, 100 \text{ m}]$, and the physical parameters appearing in the seismic wave equations 5 and 6 are taken as the values for material 1 defined in Table 1. We will consider a relatively small simulation time, so that no reflection is created from the boundary of the domain, and therefore a zero boundary condition for the velocity is assumed. We choose a point source that is vertically excited at $[140 \text{ and } 0 \text{ m}]$. For the numerical computations using our SDG method, we take the mesh size as $h = 0.167 \text{ m}$ and the time step size as $\Delta t = 0.033 \text{ ms}$, so that the method is stable and accurate enough. In Figure 5, we present a snapshot of vertical velocity u_2 at time $t = 0.25 \text{ s}$. From this figure, we can see the P- and

Table 1. The P- and S-wave velocities, densities, and Poisson's ratios used in our examples.

Material	V_P (m/s)	V_S (m/s)	ρ (kg m^{-3})	ν
1	520	300	1500	0.251
2	520	52	1500	0.495
3	160	50	1800	0.446
4	200	80	2000	0.405

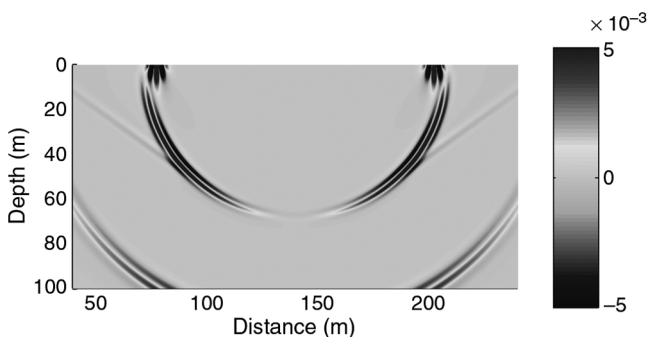


Figure 5. The snapshot for the vertical velocity u_2 at $t = 0.25 \text{ s}$ in example 1.

S-waves as well as the Rayleigh wave. In addition, the faster P-wave, which is traveling at a speed of 520 ms^{-1} , has propagated for a distance of approximately 130 m. Also, the slower S-wave, which is traveling at a speed of 300 ms^{-1} , has been propagated for a distance of approximately 75 m. On the other hand, we see that the Rayleigh wave is traveling along the free surface, and its speed is slightly smaller than that of the S-wave. To show the accuracy of the SDG method, we compare the solution obtained by the SDG method and a reference solution obtained by a fourth-order staggered-grid FDM on a very fine mesh. In Figure 6, we present this comparison at four different observation points (160 and 5 m), (180 and 5 m), (200 and 5 m), and (220 and 5 m), where the blue curve represents the SDG solution and the red dashed line represents the reference solution. From these comparisons, we see clearly that the SDG method gives a very accurate solution. In Figure 7, we present the ability of the SDG method in preserving the wave energy by computing the relative rate of change of energy over time, which is defined as

$$\delta(t) = \frac{1}{E_\infty} \frac{dE}{dt}, \quad (71)$$

where the energy $E(t)$ is given by

$$E(t) = \frac{1}{2} \int_{\Omega} (\rho u_1^2 + \rho u_2^2 + \sigma^T A \sigma) dx, \quad (72)$$

and E_∞ is the total amount of energy created by the point source. As we can see in Figure 7, the source enters into the computational domain between the initial time and 0.05 ms. After this time, we see clearly that the relative rate of change of energy $\delta(t)$ remains zero, confirming the energy conservation property of our scheme. In Figure 8, we present a comparison of seismograms for our SDG solution and the reference solution at the depth $z = 5 \text{ m}$ for times up to 0.25 s. We again see that our method performs well.

In example 2, we simulate the S-wave and the Rayleigh wave for a material with higher Poisson's ratio. The domain of interest is $[5, 45 \text{ m}] \times [0, 15 \text{ m}]$. The physical parameters appearing in the seismic-wave equations 5 and 6 are taken as the values for material 2 defined in Table 1. We also apply the multiaxial PMLs (MPMLs) (see, e.g., Meza-Fajardo and Papageorgiou, 2008) with a 5 m width on the boundary of the domain except the free surface. A point source is vertically excited at $[10 \text{ and } 0 \text{ m}]$. For the numerical computations by our SDG method, the mesh size $h = 0.05 \text{ m}$ and the time step size $\Delta t = 0.01 \text{ ms}$. Snapshots for u_2 at times 0.2, 0.4, and 0.6 s are shown in Figure 9, where the black lines represent the interface between the computational domain and the MPMLs. First of all, we see that the fast P-wave, with a velocity of 520 m/s, has already left the computational domain. With the MPML, the P-wave leaves the domain without much artificial reflection. Moreover, we can see clearly the slower S-wave and the Rayleigh wave near the surface. The S-wave reaches the lower boundary of the domain and is absorbed by the MPML. In addition, we show the comparison of our solution to the reference solution obtained by a fourth-order finite-difference scheme on a very fine mesh at some observation points in Figure 10. It is evident that our SDG method is able to produce accurate numerical solutions, and it preserves the wave energy well. We remark that the SDG solution travels a little bit slower than the reference solution, which is due to numerical

dispersion. We will discuss more about numerical dispersion at the end of this section.

In our third example, called example 3, we will stimulate Rayleigh waves in a heterogeneous material with vertical variations in velocity structure on scales smaller than a wavelength. The domain of interest is $[20, 260 \text{ m}] \times [0, 120 \text{ m}]$. Moreover, the density is 1500 kgm^{-3} , and the P- and S-wave velocities are described in

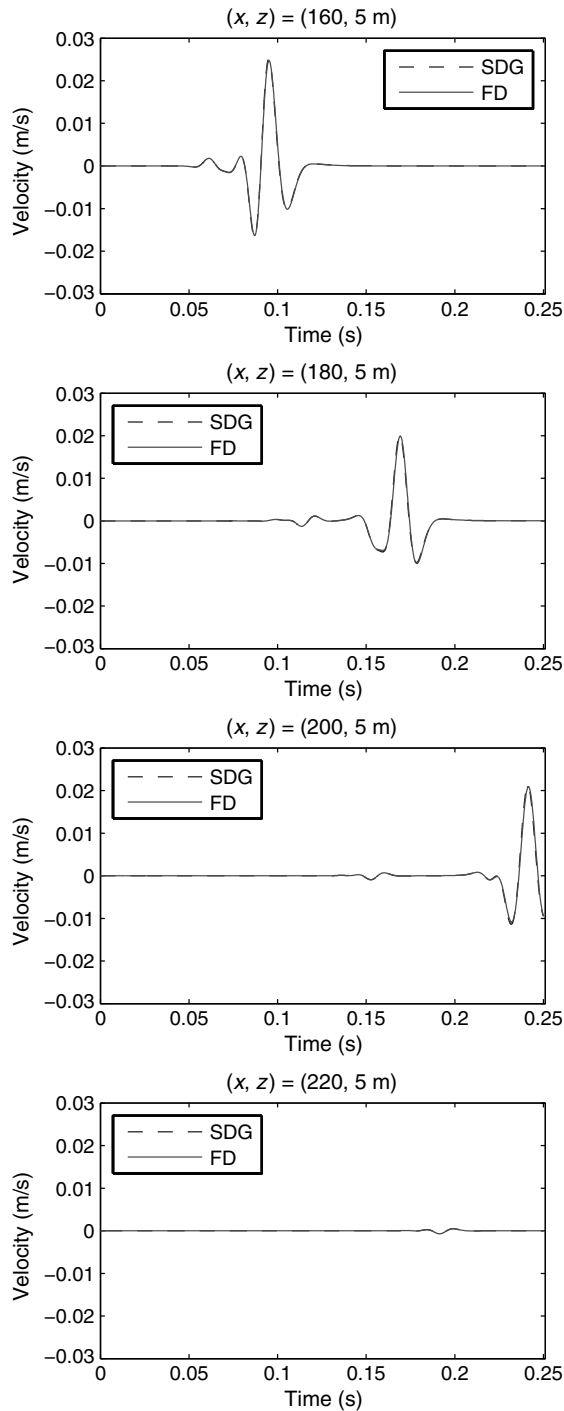


Figure 6. Comparison of our solution (SDG) to a reference solution at various observation points in example 1.

Figure 11. For the numerical computations, we will apply zero boundary conditions at $x = 0$ and 280 m . The mesh size is taken as 0.2 m , and the time step size is taken according to the stability condition presented in the previous section. A point source is vertically excited at $[140 \text{ and } 0 \text{ m}]$, and the snapshot of the solution u_2 at the simulation time $T = 0.4 \text{ s}$ is shown in Figure 12. From this figure, we see clearly the dispersive behavior of the Rayleigh wave for a vertically varying velocity model is accurately captured. In addition, a comparison of seismograms of the SDG solution and a refer-

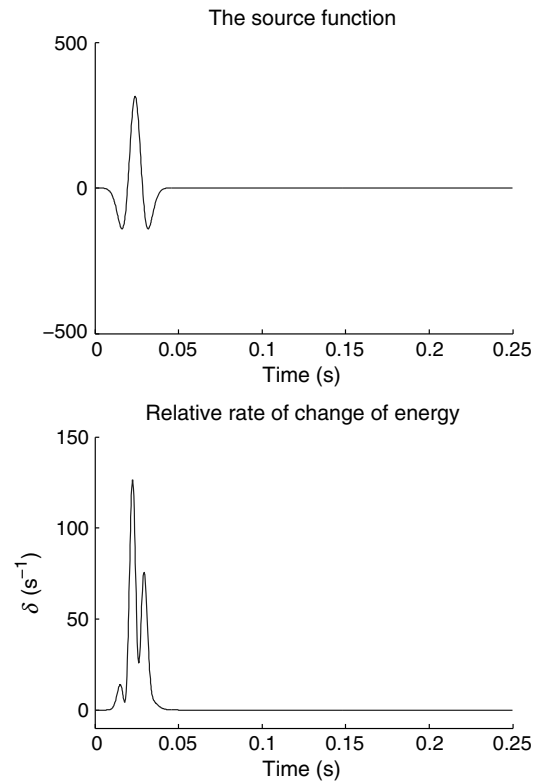


Figure 7. The source function and the relative rate of change of the energy over time in example 1.

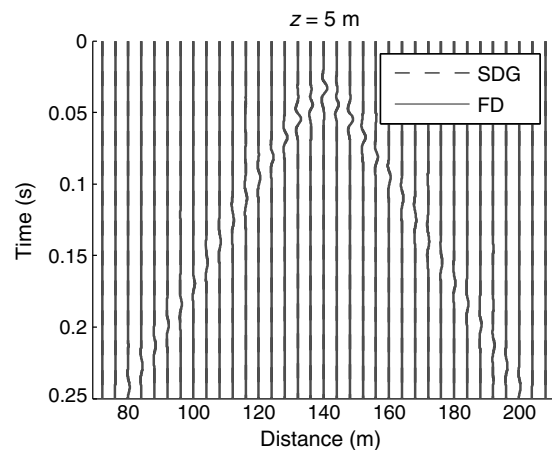


Figure 8. Comparison of seismograms with the SDG and the reference solutions for example 1.

ence solution is shown in Figure 13. Despite some small differences, we can see that the two solutions have a very good match.

In examples 4 and 5, we demonstrate the ability of our scheme to simulate Rayleigh waves in a domain with surface topography. We assume again that the physical parameters appearing in the seismic-wave equations 5 and 6 are taken as the values for material 2 defined in Table 1. In example 4, the surface topography is mathematically modeled by the function $\Gamma_4(x) = -4 \exp(-\frac{(x-8)^2}{20})$ and is a convex shaped surface. The computational domain and the MPML are depicted in Figure 13. The point source is vertically excited at [8 and -4 m], which is at the top part of the convex region of the free surface. For the numerical computations by our SDG method, the mesh size $h = 0.05$ m and the time step size is $\Delta t = 3.33 \mu\text{s}$ to ensure stability and accuracy. We also apply the MPML with a 5 m width to absorb outgoing waves. The snapshots of u_2 at times $t = 0.1, 0.3$, and $t = 0.5$ s are shown in Figure 14. First, we see clearly that the fast P-wave has already left the domain and that the MPML successfully absorbs the outgoing P-wave. On the other hand, the slower S-wave and the Rayleigh wave near the free surface are accurately simulated. We also see that the S-wave is successfully absorbed by the MPML in the left and the lower layers.

In example 5, the surface topography is modeled by the function $\Gamma_5(x) = 3 \exp(-\frac{(x-20)^2}{20})$ and is a concave-shaped surface. The computational domain and the MPML are depicted in Figure 15. The point source is vertically excited at [6 and 0 m], which is on the part of the flat surface located on the left of the concave free surface. For the numerical computations by our SDG method, the mesh size $h = 0.05$ m, the time step size is $\Delta t = 0.006$ ms, and MPML is also used to absorb outgoing waves. The snapshots of

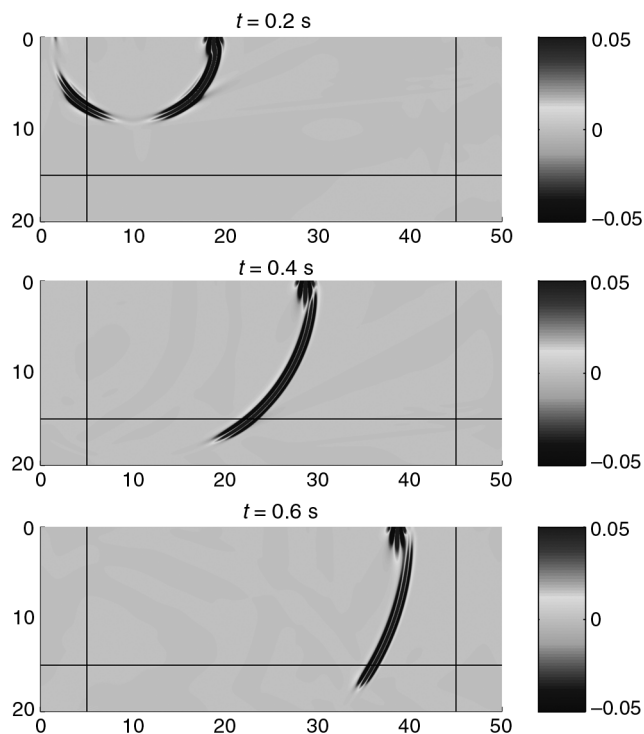


Figure 9. Snapshots for the vertical velocity u_2 in example 2. The black lines indicate the interface between the domain of interest and the MPMLs.

u_2 at times $t = 0.1, 0.3$, and 0.5 s are shown in Figure 15. We observe a similar behavior as in example 4.

In example 6, we consider the surface topography and internal discontinuities. The surface topology is given by $\Gamma_6(x) = -4 \exp(-\frac{(x-8)^2}{20})$, which is the same as Γ_4 in example 4. The internal interface between the two layers of different materials is given by $\Gamma_6(x) + 8$. This definition can be seen in Figure 16, where the dot-

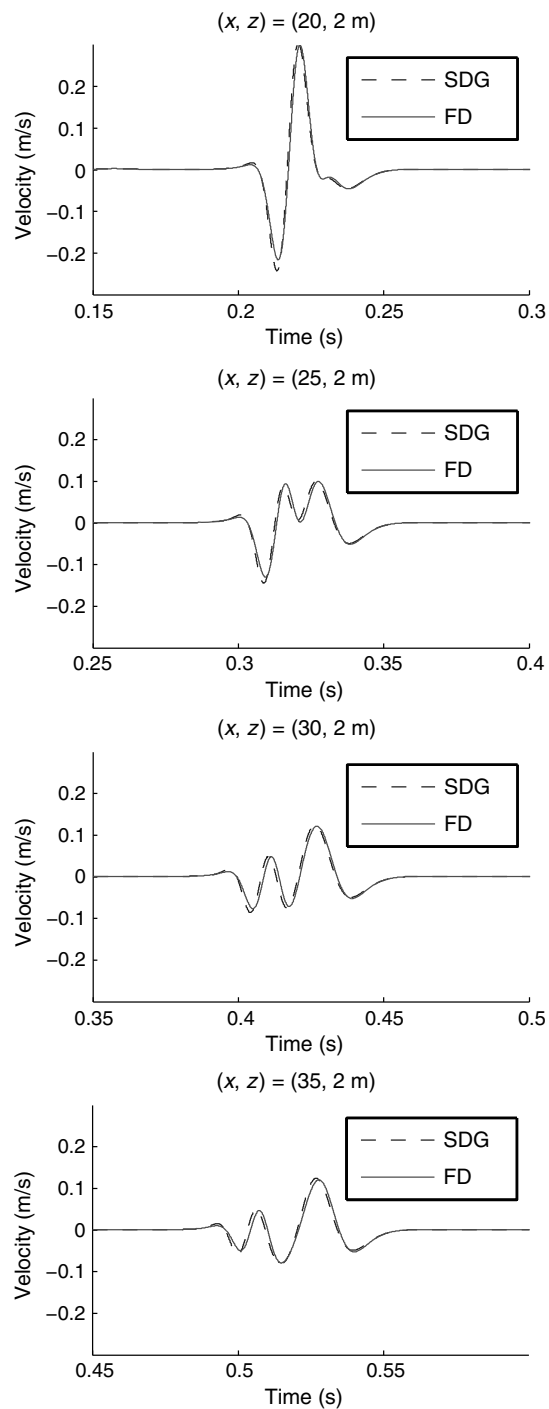


Figure 10. Comparison of our solution (SDG) to a reference solution at various observation points in example 2.

ted lines represent the interface between the two materials. The upper layer consists of material 3 and the lower layer consists of material 4 in Table 1, respectively. For the computations by the SDG method, the mesh size is $h = 0.10$ m and the time step size is 0.0125 ms, so that the method is stable and accurate. The snapshots of the solution u_2 at times $t = 0.05, 0.2, 0.3,$ and 0.4 s are shown in Figure 16. First, we see that the S-wave and the Rayleigh wave are well captured. Moreover, the reflection and transmission of the waves at the internal discontinuities are accurately computed.

Numerical study of dispersion error

In this section, we present a study of the numerical dispersion of our SDG method. The study is based on the eigenvalue method used by Cohen (2002) and Chung et al. (2013a) for the acoustic- and electromagnetic-wave equations. Let $\mathbf{f} = 0$ in equation 5. We consider a plane-wave solution $e^{-i(\mathbf{k}\cdot\mathbf{x}-\omega t)}$ of equations 5 and 6, where $\mathbf{k} = (k_x, k_z)$ is the wavenumber and ω is the angular frequency. Notice that we have the following well-known dispersion relation:

$$\omega_1 = \frac{1}{\rho}(\lambda + 2\mu)(k_x^2 + k_z^2) \quad \text{and} \quad \omega_2 = \frac{1}{\rho}\mu(k_x^2 + k_z^2). \tag{73}$$

We now consider a rectangular mesh and the SDG system defined in equations 39, 40, and 42 using the piecewise linear approximation. Recall that each rectangle is divided into two triangles, which are denoted generically by $\mathcal{S}(\nu)$. For a given rectangle, we observe that

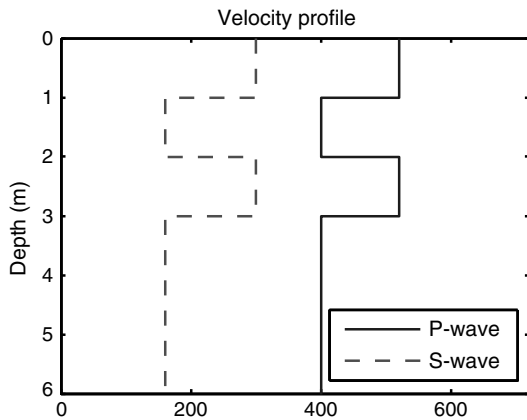


Figure 11. The velocity profiles along the depth for example 3.

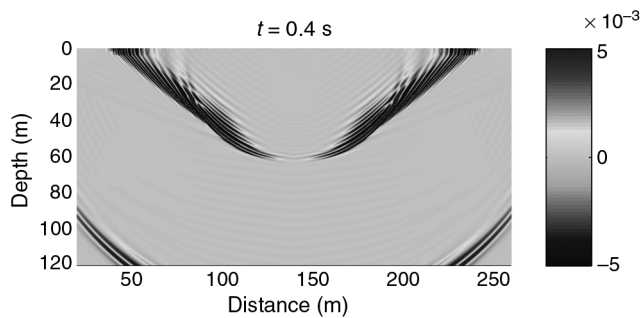


Figure 12. The snapshot for vertical velocity u_2 at $T = 0.4$ s in example 3.

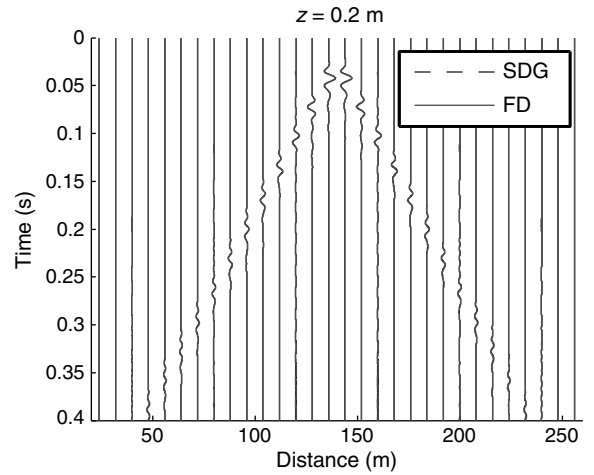


Figure 13. A comparison of seismograms of the SDG solution and a reference solution for example 3.

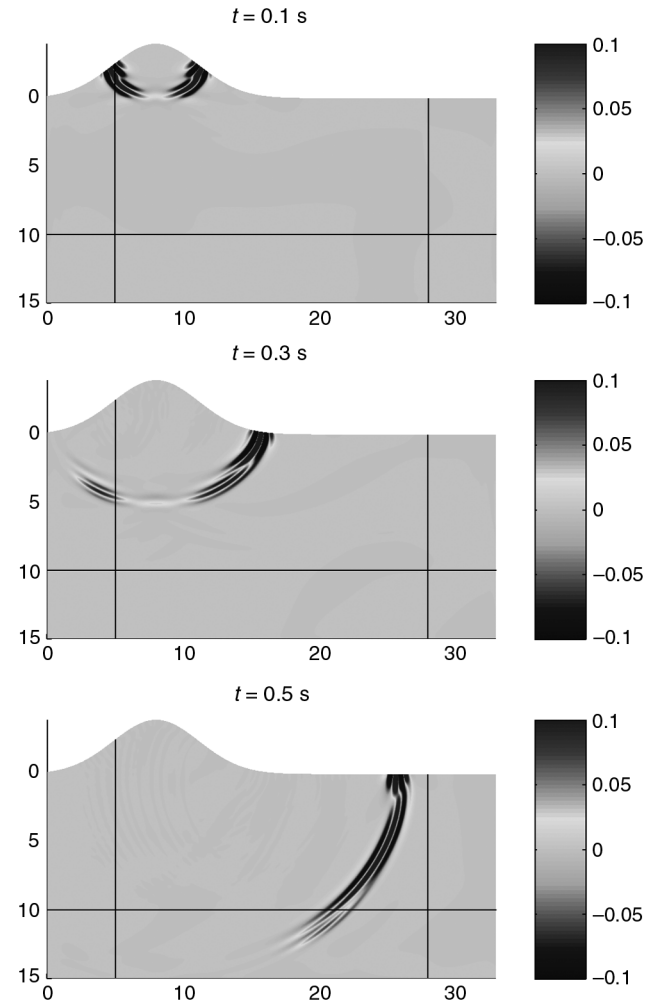


Figure 14. Snapshots for the vertical velocity u_2 in example 4. The black lines indicate the interface between the domain of interest and the MPMLs.

there are in total 24 unknowns in the variable $\tilde{\mathbf{u}}$ restricted to this rectangle, and we use \mathbf{U} to represent the vector containing these 24 unknowns. We take the time derivative in equation 39 and use equations 40 and 41 to eliminate the unknown $\tilde{\boldsymbol{\sigma}}$, we obtain the following:

$$\mathbf{A}_1 \mathbf{U}_{tt} = \mathbf{A}_2 \tilde{\mathbf{U}}, \tag{74}$$

where \mathbf{A}_1 is a block diagonal mass matrix and $\tilde{\mathbf{U}}$ is a vector containing all relevant nodal values of $\tilde{\mathbf{u}}$. To find the numerical dispersion relation, we substitute the following plane-wave solutions in equation 74:

$$u_1 = \alpha_r e^{-i(\mathbf{k}\cdot\mathbf{x} - \omega_h t)} \quad \text{and} \quad u_2 = \beta_r e^{-i(\mathbf{k}\cdot\mathbf{x} - \omega_h t)}, \tag{75}$$

where α_r and β_r only depend on the relative position of the nodal points, and ω_h is the numerical wavenumber. Then, we obtain the following generalized eigenvalue problem:

$$\omega_h^2 \tilde{\mathbf{A}}_1 \eta = \tilde{\mathbf{A}}_2 \eta. \tag{76}$$

Let Λ be the set of all generalized eigenvalues for this problem. Then, the dispersion error for ω_1 and ω_2 can be computed by

$$\min_{\omega \in \Lambda} \left| \frac{\omega_1^2}{\omega^2} - 1 \right| \quad \text{and} \quad \min_{\omega \in \Lambda} \left| \frac{\omega_2^2}{\omega^2} - 1 \right|. \tag{77}$$

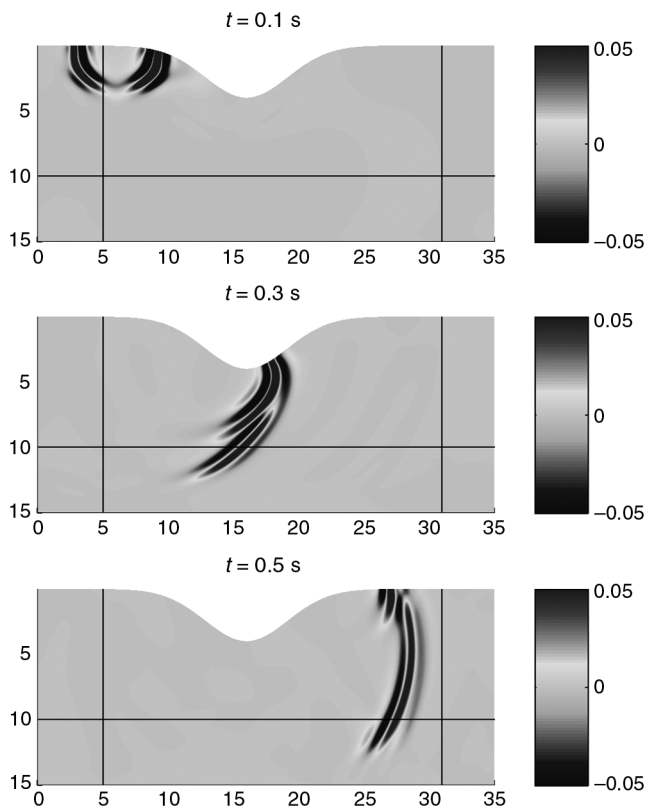


Figure 15. Snapshots for the vertical velocity u_2 in example 5. The black lines indicate the interface between the domain of interest and the MPMLs.

In Figure 17, we present the results of the SDG numerical dispersion errors using the physical parameters for material 2 defined in Table 1 and compare them with those obtained from the second and the fourth FDM. In equation 75, we take $\mathbf{k} = (\sqrt{1/3}, \sqrt{2/3})$.

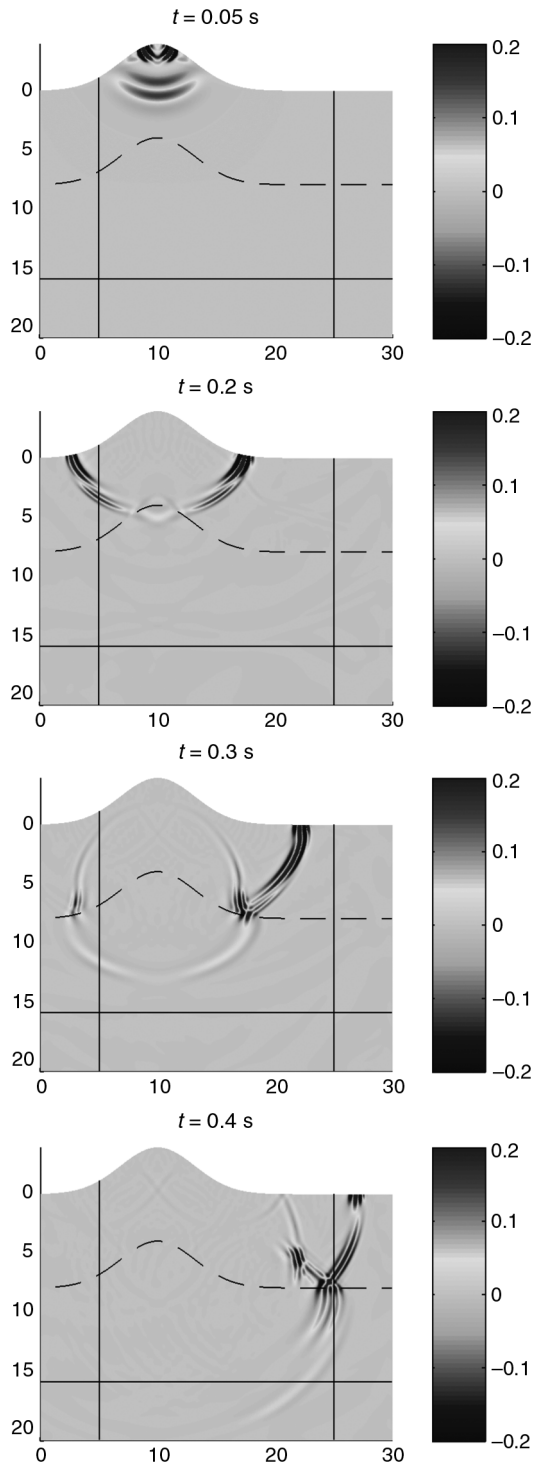


Figure 16. Snapshots for the vertical velocity u_2 in example 6. The black lines indicate the interface between the domain of interest and the MPMLs. The dotted lines indicate the interface between the two materials.

From Figure 17, we see that the dispersion error for our piecewise linear SDG method is smaller than that of the second order FDM. Being a second-order method, our SDG method performs better in terms of dispersion than second-order FDM. In addition, we see that the convergence rate of dispersion error for ω_2 is two for our SDG method and the second-order FDM. Furthermore, for ω_1 , we see that the dispersion error has a convergence order of four, which is the same convergence order for the fourth-order finite-difference scheme. We also see that the dispersion error for ω_1 for our SDG method is comparable with that of the fourth-order finite-difference scheme.

Mortar formulation

In this section, we present a strategy specifically designed for the simulation of Rayleigh waves. It is well known that the Rayleigh wave travels along the free surface and decays exponentially in the vertical direction. To make our scheme tailored to this situation, we present a mortar formulation for our SDG method. We assume that the computational domain is divided into two parts, one of them is a thin layer near the free surface. We also assume that a very fine mesh is used for this thin layer, and a coarse mesh is used in the rest of the domain. We do not assume that the meshes are matching

near the interface \mathcal{I} of these two parts of the computational domain. A schematic in Figure 18 shows this nonmatching triangulation.

Let U_h^U and U_h^L be the space for the velocity on the upper mesh and lower mesh, respectively. We assume that these two spaces are totally decoupled. We also introduce the space of Lagrange multipliers

$$\hat{U}_h = U_h^U|_{\mathcal{I}}. \quad (78)$$

We will need to modify our SDG method defined in equations 26, 28, and 29 in the following way: We note that equations 28 and 29 can be solved locally in each of the two parts of the computational domain. For equation 26, we need to decouple the velocity unknowns in the two parts of the computational domain and then enforce continuity using the above space of Lagrange multipliers. The resulting scheme reads: find $\mathbf{u}_h \in (U_h)^2$, $\boldsymbol{\Sigma}_h \in (W_h)^2$, and $\boldsymbol{\Gamma}_h \in X_h$, such that

$$\begin{aligned} \int_{\Omega} \rho \frac{\partial \mathbf{u}_h}{\partial t} \cdot \mathbf{v} dx + \int_{\mathcal{I}} \hat{\mathbf{u}}_h \cdot \mathbf{v} ds + \sum_{\kappa \in \mathcal{F}_u} \left(\int_{\mathcal{R}(\kappa)} \boldsymbol{\Sigma}_h \cdot \nabla \mathbf{v} dx \right. \\ \left. - \int_{\partial \mathcal{R}(\kappa)} (\boldsymbol{\Sigma}_h \mathbf{n}) \cdot \mathbf{v} ds \right) \\ = \int_{\Omega} \mathbf{f} \cdot \mathbf{v} dx, \quad \forall \mathbf{v} \in (U_h)^2, \hat{\mathbf{v}} \in (\hat{U}_h)^2, \\ \int_{\mathcal{I}} [\mathbf{u}_h] \cdot \hat{\mathbf{v}} ds = 0 \quad \forall \hat{\mathbf{v}} \in (\hat{U}_h)^2, \\ \int_{\Omega} \Lambda \frac{\partial \boldsymbol{\Sigma}_h}{\partial t} \cdot \boldsymbol{\alpha} dx + \sum_{\nu \in \mathcal{N}} \left(\int_{S(\nu)} \mathbf{u}_h \operatorname{div} \boldsymbol{\alpha} dx - \int_{\partial S(\nu)} \mathbf{u}_h \cdot (\boldsymbol{\alpha} \mathbf{n}) ds \right) \\ + \int_{\Omega} \boldsymbol{\Gamma}_h \cdot \boldsymbol{\alpha} dx = 0, \quad \forall \boldsymbol{\alpha} \in (W_h)^2, \\ \int_{\Omega} \boldsymbol{\Sigma}_h \cdot \boldsymbol{\eta} dx = 0, \quad \forall \boldsymbol{\eta} \in X_h, \end{aligned} \quad (79)$$

where $[\hat{\mathbf{u}}_h]$ is the jump of \mathbf{u}_h across the mesh interface \mathcal{I} . We apply this method to the same material in example 1 with same domain of interest and source position. The interface of the two meshes is located at $z = 6$ m. The mesh size for the upper mesh is 0.167 m, and

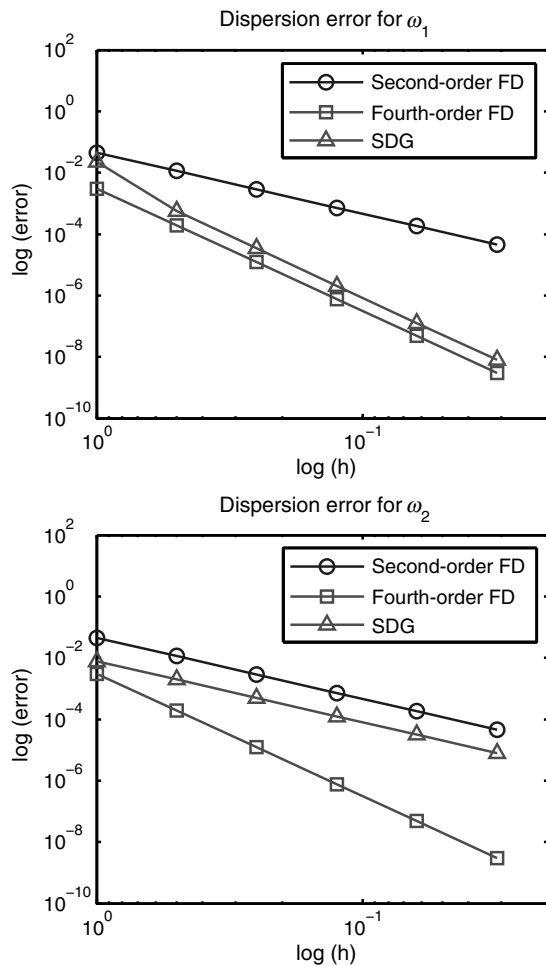


Figure 17. The comparison of dispersion error for our SDG method and finite-difference schemes.

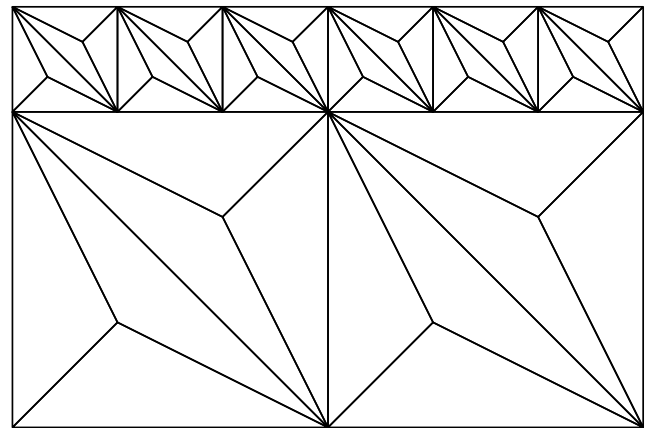


Figure 18. A nonmatching mesh used for the mortar formulation of our SDG method.

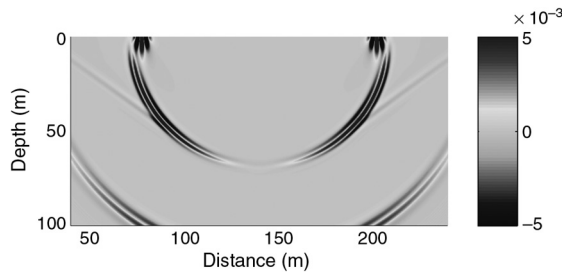


Figure 19. The snapshot for the vertical velocity u_2 at $t = 0.25$ s for the mortar formulation applying to the same model in example 1.

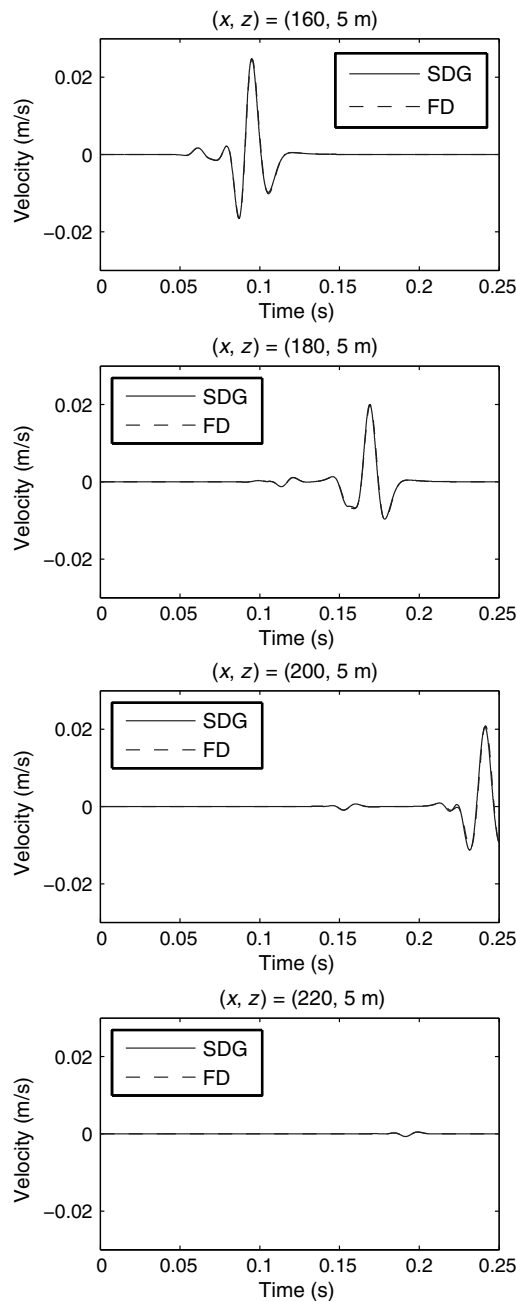


Figure 20. Comparison of the mortar solution (SDG) to a reference solution at the same observation points as in example 1.

the mesh size for the lower mesh is 0.5 m. The time step size $\Delta t = 0.033$ ms. In Figure 19, we present the snapshot of solution u_2 at time $t = 0.25$ s, and in Figure 20, we present a comparison of the numerical solution and the reference solution at various observation points from the initial time up to time equals 0.25 s. To compare this example with example 1, we compute the relative error defined by $\frac{\|u_2 - u_{2,ref}\|_2}{\|u_{2,ref}\|_2}$ at $z = 5$ m and $0 \leq t \leq 0.25$ s, where $u_{2,ref}$ is the reference solution for u_2 . The relative error for example 1 and the mortar example is 0.18% and 0.22%, respectively. The results show that the mortar formulation produces equally accurate results. Moreover, in the current setting in which the coarse mesh size is three times larger than the fine mesh size, the speed up is approximately 5.2 times.

CONCLUSIONS

We have developed an SDG method for the velocity-stress formulation of elastic waves. Moreover, by a mortar formulation, our method can be used for the simulations of Rayleigh waves. The method enjoys several distinctive features that are particularly attractive: First, it conserves the wave energy automatically; second, it is optimally convergent in the L^2 -norm and the energy norm; third, only solutions of a block diagonal linear system and a local saddle point system are needed in each time step, giving a very efficient time marching scheme; fourth, it is flexible in handling complex geometries, so that free surface conditions on nonflat surfaces can be imposed easily; and fifth, it yields solutions with extremely low dispersion errors. Numerical examples have shown that the SDG method provides a competitive alternative for simulations of seismic and Rayleigh waves with irregular surface topography.

ACKNOWLEDGMENTS

The research of E. Chung is partially supported by Hong Kong Research Grant Council General Research Fund (Project: 400813) and the Chinese University of Hong Kong Direct Grant for Research (2013/14). The research of J. Qian is partially supported by the National Science Foundation.

REFERENCES

- Ainsworth, M., P. Monk, and W. Muniz, 2006, Dispersive and dissipative properties of discontinuous Galerkin finite element methods for the second-order wave equation: *Journal of Scientific Computing*, **27**, 5–40, doi: [10.1007/s10915-005-9044-x](https://doi.org/10.1007/s10915-005-9044-x).
- Aki, K., and P. G. Richards, 2002, *Quantitative seismology*: University Science Books.
- Appelö, D., and N. A. Petersson, 2009, A stable finite difference method for the elastic wave equation on complex geometries with free surfaces: *Communications in Computational Physics*, **5**, 84–107.
- Arnold, D. N., 1982, An interior penalty finite element method with discontinuous elements: *SIAM Journal on Numerical Analysis*, **19**, 742–760, doi: [10.1137/0719052](https://doi.org/10.1137/0719052).
- Basabe, J. D., and M. K. Sen, 2009, New developments in the finite-element method for seismic modeling: *The Leading Edge*, **28**, 562–567, doi: [10.1190/1.3124931](https://doi.org/10.1190/1.3124931).
- Becache, E., P. Joly, and C. Tsogka, 2000, An analysis of new mixed finite elements for the approximation of wave propagation problems: *SIAM Journal on Numerical Analysis*, **37**, 1053–1084, doi: [10.1137/S0036142998345499](https://doi.org/10.1137/S0036142998345499).
- Bernacki, M., S. Lanteri, and S. Piperno, 2006, Time-domain parallel simulation of heterogeneous wave propagation on unstructured grids using explicit, nondiffusive, discontinuous Galerkin methods: *Journal of Computational Acoustics*, **14**, 57–81, doi: [10.1142/S0218396X06002937](https://doi.org/10.1142/S0218396X06002937).

- Bohlen, T., and E. H. Saenger, 2006, Accuracy of heterogeneous staggered-grid finite-difference modeling of Rayleigh waves: *Geophysics*, **71**, no. 4, T109–T115, doi: [10.1190/1.2213051](https://doi.org/10.1190/1.2213051).
- Bourdel, F., P.-A. Mazet, and P. Helluy, 1991, Resolution of the non-stationary or harmonic Maxwell equations by a discontinuous finite element method: Application to an E.M.I. (electromagnetic impulse) case, in R. Glowinski, ed., *Proceedings of the 10th International Conference on Computing Methods in Applied Sciences and Engineering*: Nova Science Publishers, Inc., 405–422.
- Chan, H., E. Chung, and G. Cohen, 2013, Stability and dispersion analysis of staggered discontinuous Galerkin method for wave propagation: *International Journal of Numerical Analysis and Modeling*, **10**, 233–256.
- Chung, E., and P. Ciarlet, 2013, A staggered discontinuous Galerkin method for wave propagation in media with dielectrics and meta-materials: *Journal of Computational and Applied Mathematics*, **239**, 189–207, doi: [10.1016/j.cam.2012.09.033](https://doi.org/10.1016/j.cam.2012.09.033).
- Chung, E., P. Ciarlet, and T. F. Yu, 2013a, Convergence and superconvergence of staggered discontinuous Galerkin methods for the three-dimensional Maxwell's equations on Cartesian grids: *Journal of Computational Physics*, **235**, 14–31, doi: [10.1016/j.jcp.2012.10.019](https://doi.org/10.1016/j.jcp.2012.10.019).
- Chung, E., B. Cockburn, and G. Fu, 2014a, The staggered DG method is the limit of a hybridizable DG method: *SIAM Journal on Numerical Analysis*, **52**, 915–932, doi: [10.1137/13091573X](https://doi.org/10.1137/13091573X).
- Chung, E., and B. Engquist, 2006, Optimal discontinuous Galerkin methods for wave propagation: *SIAM Journal on Numerical Analysis*, **44**, 2131–2158, doi: [10.1137/050641193](https://doi.org/10.1137/050641193).
- Chung, E., and B. Engquist, 2009, Optimal discontinuous Galerkin methods for the acoustic wave equation in higher dimensions: *SIAM Journal on Numerical Analysis*, **47**, 3820–3848, doi: [10.1137/080729062](https://doi.org/10.1137/080729062).
- Chung, E., and H. Kim, 2014, A deluxe FETI-DP algorithm for a hybrid staggered discontinuous Galerkin method for H(curl)-elliptic problems: *International Journal for Numerical Methods in Engineering*, **98**, 1–23, doi: [10.1002/nme.4617](https://doi.org/10.1002/nme.4617).
- Chung, E., H. Kim, and O. Widlund, 2013b, Two-level overlapping Schwarz algorithms for a staggered discontinuous Galerkin method: *SIAM Journal on Numerical Analysis*, **51**, 47–67, doi: [10.1137/110849432](https://doi.org/10.1137/110849432).
- Chung, E., and C. Lee, 2012, A staggered discontinuous Galerkin method for the curl-curl operator: *IMA Journal of Numerical Analysis*, **32**, 1241–1265, doi: [10.1093/imanum/drr039](https://doi.org/10.1093/imanum/drr039).
- Chung, E., M. Yuen, and L. Zhong, 2014b, A-posteriori error analysis for a staggered discontinuous Galerkin discretization of the time-harmonic Maxwell's equations: *Applied Mathematics and Computation*, **237**, 613–631.
- Cockburn, B., G. E. Karniadakis, and C.-W. Shu, 2000, *Discontinuous Galerkin methods: Theory, computation and applications*: Springer.
- Cohen, G., 2002, *Higher-order numerical methods for transient wave equations*: Springer.
- Cohen, G., P. Joly, N. Tordjman, and J. Roberts, 2001, Higher order triangular finite elements with mass lumping for the wave equation: *SIAM Journal on Numerical Analysis*, **38**, 2047–2078, doi: [10.1137/S0036142997329554](https://doi.org/10.1137/S0036142997329554).
- De Basabe, J. D., M. K. Sen, and M. F. Wheeler, 2008, The interior penalty discontinuous Galerkin method for elastic wave propagation: Grid dispersion: *Geophysical Journal International*, **175**, 83–93, doi: [10.1111/j.1365-246X.2008.03915.x](https://doi.org/10.1111/j.1365-246X.2008.03915.x).
- Dumbser, M., and M. Kaser, 2006, An arbitrary high-order discontinuous Galerkin method for elastic waves on unstructured meshes, Part II: The three-dimensional isotropic case: *Geophysical Journal International*, **167**, 319–336, doi: [10.1111/j.1365-246X.2006.03120.x](https://doi.org/10.1111/j.1365-246X.2006.03120.x).
- Falk, R. S., and G. R. Richter, 1999, Explicit finite element methods for symmetric hyperbolic equations: *SIAM Journal on Numerical Analysis*, **36**, 935–952, doi: [10.1137/S0036142997329463](https://doi.org/10.1137/S0036142997329463).
- Geveci, T., 1988, On the application of mixed finite element methods to the wave equation: *ESAIM Mathematical Modelling and Numerical Analysis*, **22**, 243–250.
- Giraldo, F. X., J. S. Hesthaven, and T. Warburton, 2002, Nodal high-order discontinuous Galerkin methods for the spherical shallow water equations: *Journal of Computational Physics*, **181**, 499–525, doi: [10.1006/jcph.2002.7139](https://doi.org/10.1006/jcph.2002.7139).
- Graves, R. W., 1996, Simulating seismic wave propagation in 3D elastic media using staggered-grid finite differences: *Bulletin of the Seismological Society of America*, **86**, 1091–1106.
- Grote, M. J., A. Schneebeli, and D. Schötzau, 2006, Discontinuous Galerkin finite element method for the wave equation: *SIAM Journal on Numerical Analysis*, **44**, 2408–2431, doi: [10.1137/05063194X](https://doi.org/10.1137/05063194X).
- Hestholm, S., and B. Ruud, 2002, 3D free-boundary conditions for coordinate-transform finite difference seismic modelling: *Geophysical Prospecting*, **50**, 463–474, doi: [10.1046/j.1365-2478.2002.00327.x](https://doi.org/10.1046/j.1365-2478.2002.00327.x).
- Hu, F. Q., M. Y. Hussaini, and P. Rasetarinera, 1999, An analysis of the discontinuous Galerkin method for wave propagation problems: *Journal of Computational Physics*, **151**, 921–946, doi: [10.1006/jcph.1999.6227](https://doi.org/10.1006/jcph.1999.6227).
- Johnson, C., and J. Pitkäranta, 1986, An analysis of the discontinuous Galerkin method for a scalar hyperbolic equation: *Mathematics of Computation*, **46**, 1–26, doi: [10.1090/S0025-5718-1986-0815828-4](https://doi.org/10.1090/S0025-5718-1986-0815828-4).
- Kim, H., E. Chung, and C. Lee, 2013, A staggered discontinuous Galerkin method for the Stokes system: *SIAM Journal on Numerical Analysis*, **51**, 3327–3350, doi: [10.1137/120896037](https://doi.org/10.1137/120896037).
- Kim, H., E. Chung, and C. Lee, 2014, A BDDC algorithm for a class of staggered discontinuous Galerkin methods: *Computers and Mathematics with Applications*, **67**, 1373–1389, doi: [10.1016/j.camwa.2014.02.001](https://doi.org/10.1016/j.camwa.2014.02.001).
- Komatitsch, D., F. Couteil, and P. Mora, 1996, Tensorial formulation of the wave equation for modelling curved interfaces: *Geophysical Journal International*, **127**, 156–168, doi: [10.1111/j.1365-246X.1996.tb01541.x](https://doi.org/10.1111/j.1365-246X.1996.tb01541.x).
- Komatitsch, D., J. Labarta, and D. Michea, 2008, A simulation of seismic wave propagation at high resolution in the inner core of the earth on 2166 processors of MareNostrum, in J. M. Laginha, M. Palma, P. R. Amestoy, M. Daydé, M. Mattoso, and J. C. Lopes, eds., *High performance computing for computational science — VECPAR*: Springer, Lecture Notes in Computer Science 5336, 364–377.
- Komatitsch, D., and J. P. Vilotte, 1998, The spectral-element method: An efficient tool to simulate the seismic response of 2D and 3D geological structures: *Bulletin of the Seismological Society of America*, **88**, 368–392.
- Kosloff, D., and J. M. Carcione, 2010, Two-dimensional simulation of Rayleigh waves with staggered sine/cosine transforms and variable grid spacing: *Geophysics*, **75**, no. 4, T133–T140, doi: [10.1190/1.3429951](https://doi.org/10.1190/1.3429951).
- Lesaint, P., and P. A. Raviart, 1974, On a finite element method for solving the neutron transport equation (proc. Symposium, mathematical research center): in C. de Boor, ed., *Mathematical aspects of finite elements in partial differential equations*: Academic Press 8, 89–123.
- Levander, A. R., 1988, Fourth-order finite-difference P-SV seismograms: *Geophysics*, **53**, 1425–1436, doi: [10.1190/1.1442422](https://doi.org/10.1190/1.1442422).
- Lombard, B., J. Piraux, C. Gélis, and J. Virieux, 2008, Free and smooth boundaries in 2-D finite difference schemes for transient elastic waves: *Geophysical Journal International*, **172**, 252–261, doi: [10.1111/j.1365-246X.2007.03620.x](https://doi.org/10.1111/j.1365-246X.2007.03620.x).
- Ma, S., R. J. Archuleta, and P. Liu, 2004, Hybrid modeling of elastic P-SV wave motion: A combined finite-element and staggered-grid finite-difference approach: *Bulletin of the Seismological Society of America*, **94**, 1557–1563, doi: [10.1785/012003087](https://doi.org/10.1785/012003087).
- Madariaga, R., 1976, Dynamics of an expanding circular fault: *Bulletin of the Seismological Society of America*, **66**, 639–666.
- Meza-Fajardo, K., and A. Papageorgiou, 2008, A nonconvolutional, split-field, perfectly matched layer for wave propagation in isotropic and anisotropic elastic media: Stability analysis: *Bulletin of the Seismological Society of America*, **98**, 1811–1836, doi: [10.1785/0120070223](https://doi.org/10.1785/0120070223).
- Moczo, P., E. Bystrický, J. Kristek, J. M. Carcione, and M. Bouchon, 1997, Hybrid modeling of P-SV seismic motion at inhomogeneous viscoelastic topographic structures: *Bulletin of the Seismological Society of America*, **87**, 1305–1323.
- Patera, A. T., 1984, A spectral element method for fluid dynamics: Laminar flow in a channel expansion: *Journal of Computational Physics*, **54**, 468–488, doi: [10.1016/0021-9991\(84\)90128-1](https://doi.org/10.1016/0021-9991(84)90128-1).
- Raviart, P. A., and J. M. Thomas, 1977, A mixed finite element method for second order problems, in I. Galligani, and E. Magenes, eds., *Mathematical aspects of finite element methods*, Lecture notes in mathematics 606, Springer, 292–315.
- Reed, W. H., and T. R. Hill, 1973, *Triangular mesh methods for the neutron transport equation*: Technical Report LA-UR-73-479, Los Alamos Scientific Laboratory.
- Riviere, B. M., 2008, *Discontinuous Galerkin methods for solving elliptic and parabolic equations: Theory and implementation*: SIAM.
- Rivière, B., and M. F. Wheeler, 2003, Discontinuous finite element methods for acoustic and elastic wave problems: *Contemporary Mathematics*, **329**, 271–282, doi: [10.1090/conm/329](https://doi.org/10.1090/conm/329).
- Robertsson, J. O., 1996, A numerical free-surface condition for elastic/viscoelastic finite-difference modeling in the presence of topography: *Geophysics*, **61**, 1921–1934, doi: [10.1190/1.1444107](https://doi.org/10.1190/1.1444107).
- Seriani, G., and E. Priolo, 1994, Spectral element method for acoustic wave simulation in heterogeneous media: *Finite Element in Analysis and Design*, **16**, 337–348.
- Stenberg, R., 1988, A family of mixed finite elements for the elasticity problem: *Numerische Mathematik*, **53**, 513–538, doi: [10.1007/BF01397550](https://doi.org/10.1007/BF01397550).
- Virieux, J., 1986, P-SV wave propagation in heterogeneous media: Velocity-stress finite-difference method: *Geophysics*, **51**, 889–901, doi: [10.1190/1.1442147](https://doi.org/10.1190/1.1442147).
- Zahradnik, J., P. Moczo, and F. Hron, 1993, Testing four elastic finite-difference schemes for behavior at discontinuities: *Bulletin of the Seismological Society of America*, **83**, 107–129.
- Zeng, C., J. Xia, R. D. Miller, and G. P. Tsosflis, 2012, An improved vacuum formulation for 2D finite-difference modeling of Rayleigh waves including surface topography and internal discontinuities: *Geophysics*, **77**, no. 1, T1–T9, doi: [10.1190/geo2011-0067.1](https://doi.org/10.1190/geo2011-0067.1).
- Zhang, W., and X. Chen, 2006, Traction image method for irregular free surface boundaries in finite difference seismic wave simulation: *Geophysical Journal International*, **167**, 337–353, doi: [10.1111/j.1365-246X.2006.03113.x](https://doi.org/10.1111/j.1365-246X.2006.03113.x).